










## RESEARCH ARTICLE

10.1029/2021JD035658

# Modeling the Transport and Deposition of $^{10}\text{Be}$ Produced by the Strongest Solar Proton Event During the Holocene

T. C. Spiegl<sup>1,2</sup> , S. Yoden<sup>2,3</sup> , U. Langematz<sup>1</sup>, T. Sato<sup>4</sup> , R. Chhin<sup>2,5</sup> , S. Noda<sup>2</sup> , F. Miyake<sup>6</sup> , K. Kusano<sup>6</sup> , K. Schaar<sup>1</sup>, and M. Kunze<sup>1,7</sup>

<sup>1</sup>Institut für Meteorologie, Freie Universität Berlin, Berlin, Germany, <sup>2</sup>Graduate School of Science, Kyoto University, Kyoto, Japan, <sup>3</sup>Institute for Liberal Arts and Sciences, Kyoto University, Kyoto, Japan, <sup>4</sup>Japan Atomic Energy Agency, Tokai, Japan, <sup>5</sup>Water and Environmental Unit, Research and Innovation Center, Institute of Technology of Cambodia, Cambodia, <sup>6</sup>Institute for Space-Earth Environmental Research, Nagoya University, Nagoya, Japan, <sup>7</sup>Leibniz Institute of Atmospheric Physics, Kühlungsborn, Germany

### Key Points:

- The modeled transport and deposition of the cosmogenic nuclide  $^{10}\text{Be}$  produced by the 774/775 solar proton event was compared to  $^{10}\text{Be}$  ice core records
- Hemispheric differences in stratospheric and cross-tropopause transport, and deposition were identified, with polar summertime maxima of  $^{10}\text{Be}$  surface flux
- Differences in reconstructed  $^{10}\text{Be}$  surface fluxes are explained by the local ratio of wet to dry deposition maximizing in the summertime

### Correspondence to:

T. C. Spiegl,  
[tobias.spiegl@met.fu-berlin.de](mailto:tobias.spiegl@met.fu-berlin.de)

### Citation:

Spiegl, T. C., Yoden, S., Langematz, U., Sato, T., Chhin, R., Noda, S., et al. (2022). Modeling the transport and deposition of  $^{10}\text{Be}$  produced by the strongest solar proton event during the Holocene. *Journal of Geophysical Research: Atmospheres*, 127, e2021JD035658. <https://doi.org/10.1029/2021JD035658>

Received 3 AUG 2021

Accepted 8 JUN 2022

### Author Contributions:

**Conceptualization:** T. C. Spiegl, S. Yoden, S. Noda  
**Formal analysis:** T. C. Spiegl, K. Schaar  
**Funding acquisition:** K. Kusano  
**Investigation:** T. C. Spiegl, S. Yoden  
**Methodology:** T. C. Spiegl, S. Yoden, U. Langematz, T. Sato  
**Project Administration:** K. Kusano  
**Resources:** T. C. Spiegl, S. Yoden, T. Sato, F. Miyake, M. Kunze  
**Software:** T. C. Spiegl, T. Sato  
**Supervision:** K. Kusano  
**Validation:** T. C. Spiegl  
**Visualization:** T. C. Spiegl

**Abstract** Prominent excursions in the number of cosmogenic nuclides (e.g.,  $^{10}\text{Be}$ ) around 774 CE/775 document the most severe solar proton event (SPE) throughout the Holocene. Its manifestation in ice cores is valuable for geochronology, but also for solar-terrestrial physics and climate modeling. Using the ECHAM/MESSy Atmospheric Chemistry (EMAC) climate model in combination with the Warning System for Aviation Exposure to SEP (WASAVIES), we investigate the transport, mixing, and deposition of the cosmogenic nuclide  $^{10}\text{Be}$  produced by the 774 CE/775 SPE. By comparing the model results to the reconstructed  $^{10}\text{Be}$  time series from four ice core records, we study the atmospheric pathways of  $^{10}\text{Be}$  from its stratospheric source to its sink at Earth's surface. The reconstructed post-SPE evolution of the  $^{10}\text{Be}$  surface fluxes at the ice core sites is well captured by the model. The downward transport of the  $^{10}\text{Be}$  atoms is controlled by the Brewer-Dobson circulation in the stratosphere and cross-tropopause transport via tropopause folds or large-scale sinking. Clear hemispheric differences in the transport and deposition processes are identified. In both polar regions the  $^{10}\text{Be}$  surface fluxes peak in summertime, with a larger influence of wet deposition on the seasonal  $^{10}\text{Be}$  surface flux in Greenland than in Antarctica. Differences in the peak  $^{10}\text{Be}$  surface flux following the 774 CE/775 SPE at the drilling sites are explained by specific meteorological conditions depending on the geographic locations of the sites.

**Plain Language Summary** During large solar storms, high energy particles are hurled with enormous force toward Earth by the Sun. As these particles collide with atmospheric constituents (such as oxygen or nitrogen) unique nuclides of cosmogenic origin are formed in the higher atmosphere. From there they are transported downwards and finally precipitate at the surface due to different sink processes. Their imprints can be conserved over thousands of years within natural archives, such as ice cores or tree rings. Analysis of these natural archives around the globe indicates that the strongest solar storm over the last 10,000 years happened around 774 CE/775. This event is estimated to have been up to two orders of magnitude stronger, than the strongest known events documented for the satellite era. In this study, we model and analyze the transport and deposition of the cosmogenic nuclides produced by the extreme 774 CE/775 event, by applying a new experimental setup. Our results might help to interpret the fingerprints of historical extreme events with respect to the prevailing atmospheric conditions.

## 1. Introduction

Sharp peaks of the cosmogenic nuclides  $^{10}\text{Be}$  and  $^{36}\text{Cl}$  around the end of the eighth century were detected in ice cores from Antarctica and Greenland (Mekhaldi et al., 2015; Miyake et al., 2015; Sigl et al., 2015). Different origins of these exceptional excursions, such as a gamma-ray burst (Hambaryan & Neuhäuser, 2013; Pavlov et al., 2013) or a cometary event (Liu et al., 2014), was discussed, but there is now consent that the sudden increase in the production of the cosmogenic nuclides was caused by an extreme solar proton event (SPE) occurring at 774 CE/775 (e.g., Mekhaldi et al., 2015; Melott & Thomas, 2012; Usoskin et al., 2013). Based on the ratio of the  $^{36}\text{Cl}$  and  $^{10}\text{Be}$  nuclides, that is, the proportion of high energy protons compared to low energy protons, Mekhaldi et al. (2015) estimated that the energy spectrum of the 774 CE/775 SPE was extremely hard. Its fluence (solar protons per  $\text{cm}^2$ ) with energies  $\geq 30$  MeV was estimated to be 25–50 times stronger than during the strongest SPE recorded by neutron monitors on 23 February 1956 (Usoskin & Kovaltsov, 2012) and 119–141 times

© 2022 The Authors.

This is an open access article under the terms of the [Creative Commons Attribution-NonCommercial License](https://creativecommons.org/licenses/by/4.0/), which permits use, distribution and reproduction in any medium, provided the original work is properly cited and is not used for commercial purposes.

**Writing – original draft:** T. C. Spiegl, S. Yoden, U. Langematz, T. Sato, S. Noda, F. Miyake, K. Kusano, M. Kunze

stronger than during the SPE on 20 January 2005 (Mekhaldi et al., 2015), the strongest event with proton fluxes >300 MeV during the satellite era. In addition to  $^{10}\text{Be}$  and  $^{36}\text{Cl}$  signatures in ice cores, the 774 CE/775 SPE also manifests in a rapid increase in the content of the  $^{14}\text{C}$  nuclide, documented first in tree rings from Yakushima, Japan (Miyake et al., 2012). Subsequent  $^{14}\text{C}$  measurements of tree samples around the world reported similar signatures of  $^{14}\text{C}$  increase around 775 CE (e.g., Gütler et al., 2015; Usoskin et al., 2013), with the maximum in  $^{14}\text{C}$  production estimated to have occurred in the boreal growing season (Büntgen et al., 2018; Uusitalo et al., 2018).

Cosmogenic nuclides are produced in the atmosphere via spallation reactions of atmospheric atoms by cosmic radiation (e.g., Masarik & Beer, 1999). A permanent source for spallation in the atmosphere is galactic cosmic rays (GCRs). The intensity of GCRs – and thus the production of cosmogenic nuclides – are modulated by solar and geomagnetic activity. Hence, variations in the abundance of cosmogenic nuclides in natural archives are shaped by the 11-year solar cycle (Usoskin et al., 2006). In contrast, SPEs happen infrequently when the Sun expels large amounts of energy and accelerates solar energetic particles (SEP) into the corona and the interplanetary medium. However, the magnitude of an individual SPE has to be extreme (in terms of the proton fluence with energy >30 MeV), in order to distinguish the number of cosmogenic nuclides produced by such an event from the background levels, produced by GCRs in proxy records. SPEs having the potential to fulfill this criterion were sparsely distributed during the last millennia (Usoskin & Kovaltsov, 2012). The latest SPE of this magnitude has been registered as so-called ground level enhancement (GLE) by neutron monitors worldwide on 20 January 2005 (Bieber et al., 2013).

The bulk of the cosmogenic nuclides (>60%) are produced in the lower stratosphere, where the combination of air density and available secondary cosmic ray products is optimal for the spallation (Heikkilä et al., 2013). After production, the cosmogenic nuclides attach quickly to sulfate aerosol particles (e.g., Junge, 1963). The aerosol-borne radionuclides are then transported with the stratospheric transport regimes, for example, the Brewer-Dobson circulation (BDC), and mixed within the stratosphere (Heikkilä et al., 2013), reaching stratospheric lifetimes in the order of one to 2 years (Feely et al., 1966). Given the much shorter lifetimes of aerosol-borne radionuclides in the troposphere – due to its more turbulent nature and deposition effects –, a large vertical gradient in the concentrations of the radionuclides exists at the tropopause which can be considered as a transport barrier. Hence, the details of the cross-tropopause transport of cosmogenic nuclides from the stratospheric reservoir to the troposphere play an important role in the measured radionuclide concentrations at the surface or in ice cores.

Stratosphere-troposphere exchange (STE) is influenced for example, by the strength of the BDC and tropospheric synoptic and mesoscale variability in the extratropics, associated with tropopause folds and cut-off lows, for example, in the vicinity of the tropospheric jets (Appenzeller et al., 1996; Holton et al., 1995; Stohl et al., 2003). Recent studies demonstrated the increasing transport of stratospheric ozone into the troposphere in a future climate (Hegglin & Shepherd, 2009; Meul et al., 2018). However, ozone – as any other chemical tracer – depends on sources and sinks (e.g., photo-chemical production and depletion) and is, moreover, influenced by anthropogenic climate change and man-made halogens. In contrast,  $^{10}\text{Be}$  atoms produced by SPEs appear pulse-like in the atmosphere. They are transported with the atmospheric circulation from the middle atmosphere (i.e., the region between the tropopause and the mesopause at about 90 km altitude) down to the troposphere, where they are ultimately removed by dry or wet deposition at the surface. Because of their long half-life of 1.4 million years, they are able to conserve the imprints of extreme SPEs in natural archives on geological timescales. These tracer characteristics are ideal to study the influence of atmospheric dynamics on the tracer distribution, and thus radionuclide measurements have been used to test the representation of STE in models (e.g., Koch & Rind, 1998).

Apart from the impact of STE, the regional distribution of cosmogenic radionuclides at the surface, conserved in terrestrial archives, is strongly influenced by deposition processes leading to the removal of the radionuclide from the troposphere. While wet deposition in regions with high precipitation rates, particularly in the middle latitudes or tropics, dominates the total deposition, the deposition rates in regions with low precipitation, like the coastal deserts in South Africa and South America, or the Antarctic and Greenland ice shields are controlled by dry deposition depending on the surface properties and local winds (Field et al., 2006; Heikkilä, 2013).

To support the interpretation of specific cosmogenic nuclide signatures in natural archives, for example, hemispheric differences, simulations with 3-dimensional global models, that include all relevant processes from the

production of the radionuclides, their transport from the stratosphere into the troposphere to their deposition at the surface, are useful tools. Apart from a good representation of STE, these models should include parameterizations of the main dry and wet deposition processes. Such model studies were, for example, performed with the NASA GISS Model E General Circulation Model (GCM) (Field et al., 2006), the ECHAM5-HAM climate model (Heikkilä, Beer, & Alfimov, 2008), or the chemistry-climate model (CCM) SOCOL (Sukhodolov et al., 2017). These studies provided important contributions to the knowledge of the atmospheric distribution and deposition patterns of the  $^{10}\text{Be}$  nuclide on the global scale. Nevertheless, discrepancies in the model results remained, for instance in the degree of global mixing of  $^{10}\text{Be}$  in the atmosphere, or the simulated concentrations of polar  $^7\text{Be}$ , which is underestimated by ECHAM5-HAM (Elsässer, 2013). This may be due to shortcomings in the applied model configurations, such as a limited vertical model domain (top level at 10 hPa) underestimating lower stratospheric variability and STE, or missing wet deposition (Sukhodolov et al., 2017).

In this study, we conducted passive tracer experiments with the ECHAM/MESSy Atmospheric Chemistry (EMAC) model (Jöckel et al., 2016) to investigate the transport and deposition of  $^{10}\text{Be}$  produced by the extreme SPE of 774 CE/775. The 3-dimensional  $^{10}\text{Be}$  initial condition was calculated for the SPE of 2005 by the operational Warning System for Aviation Exposure to SEP (WASAVIES) (Sato, Kataoka, et al., 2018) and scaled to the extreme 774 CE/775 event.

Our over-arching goal is to apply the new model setup, ECHAM/MESSy in combination with input fields used as upper boundary from WASAVIES, to support the interpretation of geochronological reconstructions from proxy data. Particularly, this study focuses on discussing:

1. the importance of the transport and mixing processes,
2. the role of the stratosphere as a reservoir in multi-year decay,
3. the role of the seasonal STE across the tropopause
4. the similarity and contrast between the two hemispheres, and
5. the relevance of the different deposition processes (wet vs. dry) in different regions.

Our new model setup combines the calculations of an operational SEP transport model with a 3-dimensional CCM to simulate the production and downward transport of  $^{10}\text{Be}$  in the middle atmosphere to the troposphere and, ultimately, its deposition at the surface. The use of a 3-dimensional model allows us to identify regional deposition patterns, including hemispheric disparities (iv), which are not captured by box model approaches that were mostly used in previous studies (e.g., Büntgen et al., 2018; Güttler et al., 2015; Miyake et al., 2014, 2012; Usoskin et al., 2013). By prescribing the  $^{10}\text{Be}$  tracer as the initial condition for the first day of each month of the year in 10 independent model simulations, an ensemble of 120 experiments was generated. Each simulation was integrated over 10 model years and analyzed including the year of injection.

We compare our model results with four ice core records from Antarctica and Greenland. This allows us to draw conclusions on the relative roles of the deposition processes in this study.

Using a complex climate model as a state-of-the-art tool, we think that our study will contribute to a better understanding of the pathways of cosmogenic nuclides from their source in the stratosphere to their deposition at Earth's surface. Our results might thus help to interpret the analysis of cosmogenic nuclides in natural archives, which are valuable landmarks for geochronology.

In Section 2 the applied models and the setup of the simulations are described. In Section 3 the simulated  $^{10}\text{Be}$  surface fluxes will be evaluated by comparison with proxy data from ice cores in Greenland and Antarctica. Sections 4 to 6 focus on the transport of the produced  $^{10}\text{Be}$  trace gas from the stratosphere across the tropopause down to Earth's surface. A detailed discussion of the reconstructed and modeled  $^{10}\text{Be}$  surface flux at the four ice core drilling sites for the 774 CE/775 SPE is presented in Section 7. Section 8 includes the final conclusions.

## 2. Models and Methods

### 2.1. The Chemistry-Climate Model EMAC

Passive tracer experiments were carried out with the ECHAM/MESSy Atmospheric Chemistry (EMAC) model (version 2.52) (Jöckel et al., 2016). EMAC is a CCM that includes sub-models describing tropospheric and middle atmospheric processes and their interaction with oceans, land, and human influences (Jöckel et al., 2010).

The atmospheric core model is the fifth generation of the European Center Hamburg general circulation model (ECHAM5; Roeckner et al., 2006). For the present study, we applied EMAC in T42L47MA-resolution, that is, with a spherical truncation of T42 (corresponding to a quadratic Gaussian grid of approx. 2.8 by 2.8° in latitude and longitude) and a vertical resolution of 47 layers (L47 with the model top at 0.01 hPa). The model setup comprises, among others, the submodel RAD/RAD-FUBRAD (Dietmüller et al., 2016) for the parameterization of radiative transfer based on Fouquart and Bonnel (1980) and Roeckner et al. (2003) (RAD). At pressures lower than 70 hPa we use the RAD-FUBRAD submodule thus increasing the spectral resolution in the UV-VIS from 1 band to 81 bands (Kunze et al., 2014; Nissen et al., 2007). The submodel QBO is used to relax the zonal wind near the equator toward prescribed zonal winds in the lower stratosphere, derived from present-day observations (Giorgetta & Bengtsson, 1999).

In our simulations, we assume that the  $^{10}\text{Be}$  atoms prescribed to the model (see Section 2.2) are soluble and get instantaneously attached to sulfate aerosols that are abundant in sufficient concentrations to saturate the complete  $^{10}\text{Be}$  loading. The  $^{10}\text{Be}$  atoms are thus transported and removed from the atmosphere as aerosol particles, having the properties of background sulfate aerosol with a density of  $1,500 \text{ kg/m}^3$ , a mean mode radius of  $R_{\text{mod}} = 0.08 \text{ }\mu\text{m}$  and distribution width of 1.6, according to present-day limb measurements with the Scanning Imaging Absorption Spectrometer for Atmospheric Chartography (Malinina et al., 2018). Sedimentation due to gravitational settling of the aerosol particles throughout the whole atmosphere is considered using a zeroth order upwind scheme (submodel SEDI) with a terminal sedimentation velocity based on the Stokes velocity corrected for aspherical particles (Kerkweg et al., 2006). Removal of aerosol particles by precipitation in the troposphere, so-called wet deposition, is parameterized by the scavenging scheme SCAV (Tost et al., 2006). The wet deposition flux of the  $^{10}\text{Be}$  aerosol particles is determined by the uptake of aerosol particles by falling rain droplets in large-scale or convective precipitation and snow (for more details see Tost et al. (2006)). Dry deposition of  $^{10}\text{Be}$  containing aerosol particles is applied at the lowest model level. The algorithm DDEP calculates dry deposition velocities depending on the near-surface turbulence and the physical and chemical properties of the surface cover for three surface types (vegetation, bare soil and snow, and water), using the big leaf approach as proposed by Wesely (1989). For more information about the dry deposition parameterization also see Ganzeveld and Lelieveld (1995), Ganzeveld et al. (1998), and Kerkweg et al. (2006).

## 2.2. Calculation of the Initial $^{10}\text{Be}$ Production Yield

Using the operational WASAVIES (Sato, Kataoka, et al., 2018) model, the initial yield of  $^{10}\text{Be}$  produced by the 774 CE/775 event,  $Y_{10\text{Be}}$ , was calculated as a function of latitude  $\varphi$ , longitude  $\theta$ , and altitude  $h$  by:

$$Y_{10\text{Be}}(\varphi, \theta, h) = \sum_{\tau=n,p} \int [\Phi_{\tau}(\varphi, \theta, h, E) N_{14\text{N}}(h) \sigma_{\tau(14\text{N}, 10\text{Be})}(E) + \Phi_{\tau}(\varphi, \theta, h, E) N_{16\text{O}}(h) \sigma_{\tau(16\text{O}, 10\text{Be})}(E)] dE$$

where  $\tau$  indicates the particle type (neutron  $n$  or proton  $p$ ),  $\Phi_{\tau}$  is the fluence (i.e., number of incident particles per  $\text{cm}^2$ ) of SEP with energy  $E$  in the atmosphere including their secondary particles,  $N_{14\text{N}}$  and  $N_{16\text{O}}$  are the concentrations of  $^{14}\text{N}$  and  $^{16}\text{O}$  in the atmosphere, respectively, and  $\sigma_{\tau(14\text{N}, 10\text{Be})}$  and  $\sigma_{\tau(16\text{O}, 10\text{Be})}$  are the production cross sections of  $^{10}\text{Be}$  from  $^{14}\text{N}$  and  $^{16}\text{O}$ , respectively.

For this study, the atmospheric concentrations of  $N_{14\text{N}}$  and  $N_{16\text{O}}$  were assumed to be independent of latitude and longitude, and their numerical values were taken from the US Standard Atmosphere, 1986 (NOAA, 1976). The production cross sections for the oxygen target  $\sigma_{\tau(16\text{O}, 10\text{Be})}$  were taken from the Lifton-Sato-Dunai model (Lifton et al., 2014), which is one of the most widely used models for scaling in-situ cosmogenic nuclide production rates. The data for the nitrogen target  $\sigma_{\tau(14\text{N}, 10\text{Be})}$  was calculated by the Particle and Heavy Ion Transport code System (PHITS) (Sato, Iwamoto, et al., 2018)

The fluence of SEP,  $\Phi_{\tau}(\varphi, \theta, h, E)$ , was calculated using the algorithm of the WASAVIES. The model determines SEP fluxes anywhere in the atmosphere using the databases based on the SEP transport simulations from the Sun to the ground level of the Earth. In WASAVIES, four free parameters have to be determined to characterize the GLE, which are the power index, the time profile of SEP generated by the Sun, the total fluence, and the tilt angle of SEP incident to the Earth. Their numerical values are calculated in real time using the proton fluxes measured by the GOES satellite and the count rates of several neutron monitors on the ground.

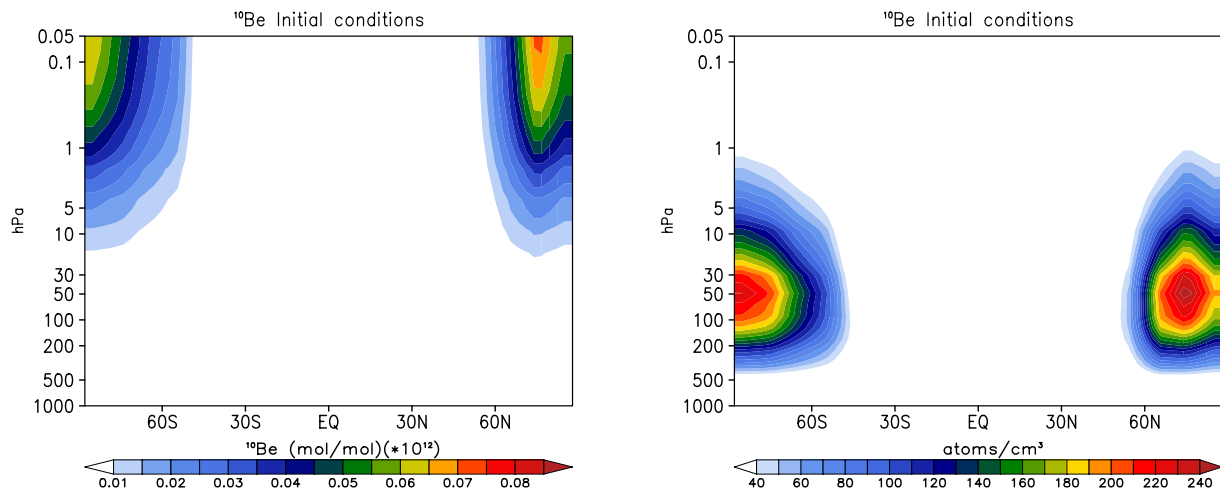


**Figure 1.** Latitude-height cross section of the  $^{10}\text{Be}$  yield from the Warning System for Aviation Exposure model used as initial field for the passive tracer experiments. Left panel:  $^{10}\text{Be}$  mixing ratio in mol/mol; right:  $^{10}\text{Be}$  concentration in atoms/cm<sup>3</sup>.

Contrary to earlier studies, we use the extreme 2005 SPE as a reference to estimate the magnitude of the 774 CE/775 event. The 2005 SPE can be regarded as the best-documented SPE within the satellite era. This is of advantage since our results rely on both, the applied scaling factor and the quality of the reference event itself.

The numerical values of these parameters for the 774 CE/775 event were set to be the same as those for GLE69 in January 2005, except for the total fluence and tilt angle of the SEP incident to the Earth. The total fluence was assumed to be 130 times larger than that derived for GLE69. This value represents a medium value in the range of scaling factors estimated by Mekhaldi et al. (2015) (119–141). Additionally, it was assumed that SEP was incident to the Earth in parallel to the ecliptic plane during the 774 CE/775 event. Figure 1 shows the height-latitude distribution of the  $Y_{10\text{Be}}$  mixing ratio (MR) (left panel) and concentration (right panel) used as the initial condition for the simulations. Whereas the  $^{10}\text{Be}$  MR maximizes in the polar mesosphere, most of the  $^{10}\text{Be}$  atoms are produced in the lower stratosphere, where the air density is higher.

As the EMAC model does not include a parameterization for the continuous  $^{10}\text{Be}$  production by galactic cosmic rays (GCRs), a mean background  $^{10}\text{Be}$  surface flux of  $0.9 \cdot 10^{-2}$  atoms/cm<sup>2</sup>/s has been derived from the four drilling sites (based on the relative years  $-5$  to  $-1$  (except for the North Greenland Ice core Project (NGRIP):  $-2$  to  $-1$ ) and  $5$ – $9$ ) and added to the simulated  $^{10}\text{Be}$  surface fluxes (e.g., in Figure 3).

### 2.3. Experimental Setup

For the passive tracer simulations of this study, EMAC was run in GCM (General Circulation Model) mode, that is, with interactive chemistry switched off. Boundary conditions for greenhouse gas concentrations and ozone depleting substances were prescribed from a preindustrial (PI) control simulation using concentrations representative for the year 1850. The solar forcing for the PI-run was chosen according to the recommendations of the SOLARIS-HEPPA initiative (Matthes et al., 2017). To exclude an impact of ozone or sea surface temperature (SST) variability on stratospheric background conditions, long-term climatologies for ozone and SSTs from the PI-run were prescribed.

The experimental setup is illustrated in Figure 2. An ensemble of 10 12-year model simulations has been performed. After a 2-year spin-up period, the  $^{10}\text{Be}$  tracer field calculated by the WASAVIES model (see Section 2.2) (Figure 1) was fed into the EMAC model at one timestep. This corresponds to a pulse-like “injection” of  $^{10}\text{Be}$  produced by the solar particles to the atmosphere after the SPE [Note that the term “injection of  $^{10}\text{Be}$ ” in the remainder of this paper will refer to the technical initialization of the  $^{10}\text{Be}$  input in the model atmosphere, corresponding to the  $^{10}\text{Be}$  production from the injection of solar particles in the real atmosphere]. The  $^{10}\text{Be}$  tracer field has been injected on the first day of each month (i.e., 12 times) of the first model year after spinup (i.e., model year 3) in each of the 10 simulations. The use of different injection months enables us to investigate the influence of the annual cycle in dynamical background conditions, while the 10-member ensemble allows us to

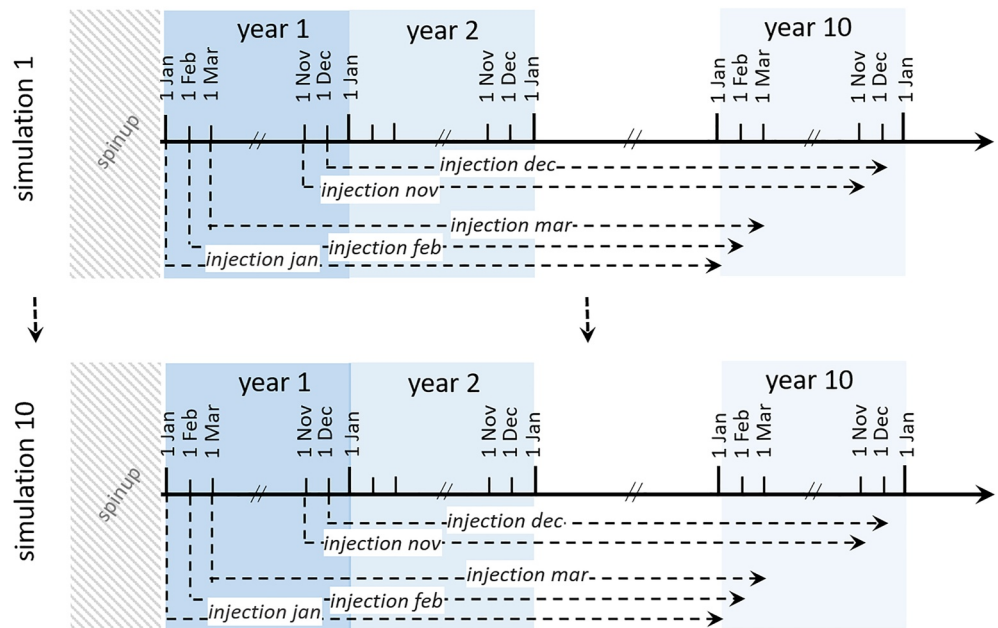


**Figure 2.** Setup of the ECHAM/MESSy Atmospheric Chemistry simulations. After a spinup period of 2 model years, each of the 10 simulations was integrated over 10 model years for analysis (year 1–10). On the first day of each month in year 1, the  $^{10}\text{Be}$  tracer field was initialized, thus producing 12 independent 10-year tracer trajectories in each of the 10 simulations.

quantify the effect of meteorological variability on the tracer transport. We thus conducted a total number of 10 (ensemble members)  $\times$  10 (analyzable years) = 100 model years. With the  $^{10}\text{Be}$  tracer initialized each month of the year, we thus obtained 120 tracer evolutions over 10 years each.

We compare our simulated surface fluxes of  $^{10}\text{Be}$  to reconstructed deposition fluxes based on ice core analyses (Mekhaldi et al., 2015; Miyake et al., 2015; Sigl et al., 2015).

#### 2.4. $^{10}\text{Be}$ Surface Flux in Greenland and Antarctica Following the 774 CE/775 SPE

One explicit goal of our work is to use the new model setup, that is, EMAC with SEP input provided by WASAV-IES, as support for the interpretation of geochronological reconstructions from proxy data by contributing physical explanations of the reconstructed data. To evaluate the performance of the simulations, we compare the model calculated  $^{10}\text{Be}$  surface flux to the latest proxy-based estimates for the years 770 CE–783. To examine hemispheric disparities, we use two ice core datasets for both Greenlandic (North Greenland Ice core Project (NGRIP) and North Greenland Eemian Ice Drilling (NEEM)) and Antarctic (West Antarctic Ice Sheet Divide Core (WDC) and Dome Fuji) drilling sites. More details for the NGRIP, NEEM, and WDC data sets are provided by Mekhaldi et al. (2015) and Sigl et al. (2015), and for the Dome Fuji data set by Miyake et al. (2015). Figure 3 shows the reconstructed  $^{10}\text{Be}$  surface flux in green with error bars representative of measuring uncertainties at the laboratory.

Note that due to differences in the age model, the Dome Fuji ice core time series has been shifted by minus 4 years to match the peak years of the other three historical sequences. In the following, we use a relative time axis with relative year 0 corresponding to the annual mean  $^{10}\text{Be}$  surface flux of the first simulation year (black solid line). Error bars for the modeled curves are calculated on the basis of the 120 tracer trajectories, which differ with respect to the monthly timing of the tracer injection. They represent the maximum and minimum responses as well as the  $\pm 1\sigma$  standard deviation. It is evident that the ensemble spread is enhanced in the first year after the tracer injection. In the following years, the uncertainties decrease at every location. This can be attributed to the fast and effective mixing of the  $^{10}\text{Be}$  tracer, leading to a homogenization of the initial height and latitudinal distribution of the  $^{10}\text{Be}$  MR during the year after the injection, as will be shown in the next section.

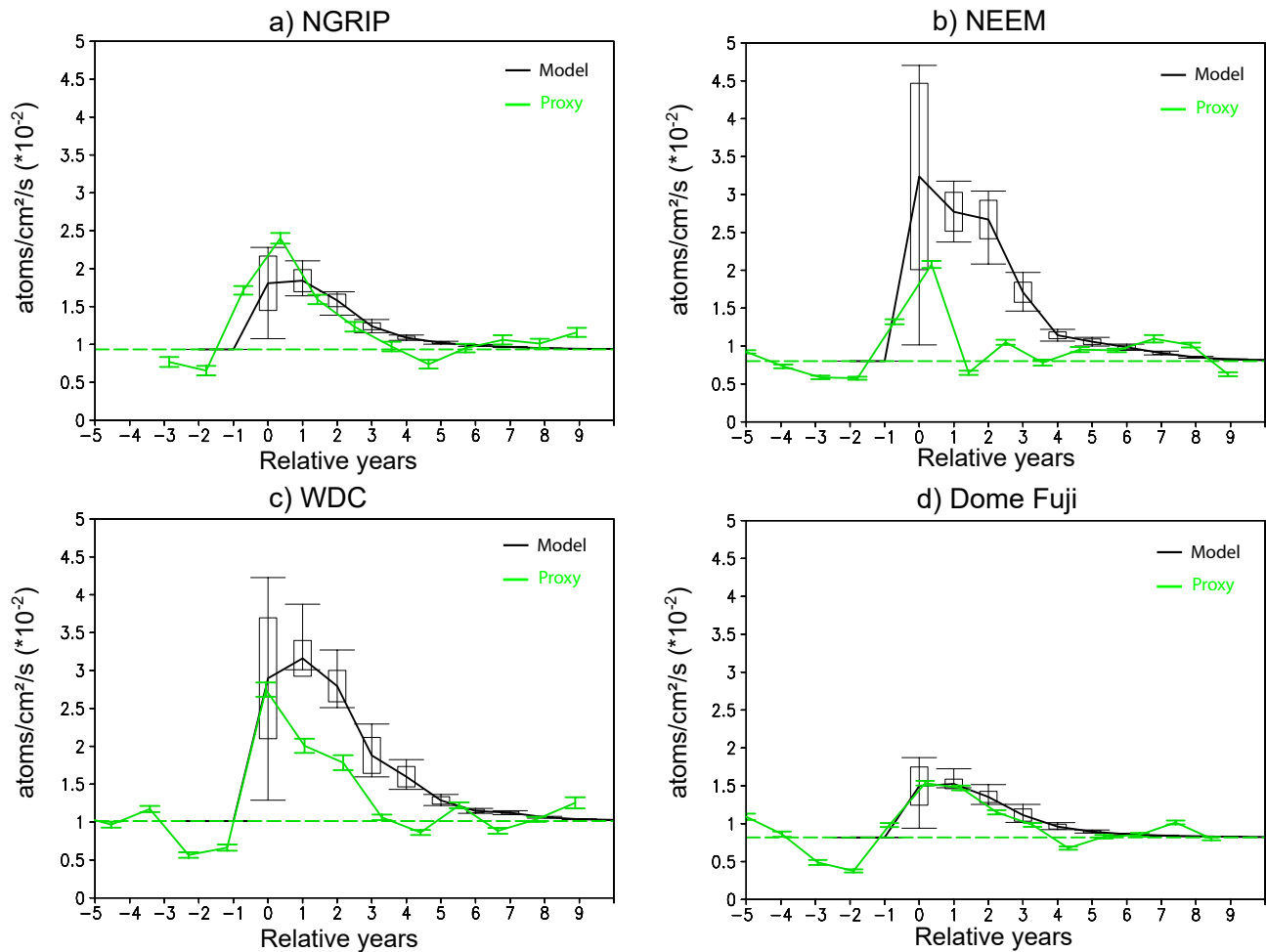


**Figure 3.** Modeled annual mean  $^{10}\text{Be}$  surface flux (black) at the (a) North Greenland Ice core Project, (b) North Greenland Ice core Project, (c) North Greenland Ice core Project and (d) Dome Fuji drilling sites. Black boxes and error bars show the standard deviation and the minimum/maximum surface flux with respect to the 10 ensemble members of the injection for each month of a year. The green curve (including error bars) represents the reconstructed surface flux (and uncertainties) from the ice core analysis. The dashed horizontal line indicates the background levels of  $^{10}\text{Be}$  surface flux for each site. Relative year 0 corresponds to the annual mean of the first model year and the peak year in the proxy data.

In general, the model seems to be able to reproduce the fast increase, the peak, and the slow decay of the reconstructed  $^{10}\text{Be}$  surface fluxes at the drilling sites, although the agreement with individual drilling sites varies. While the model ensemble mean almost perfectly matches the reconstructed  $^{10}\text{Be}$  surface fluxes at the Dome Fuji site, reconstructed peak fluxes are underestimated by the model ensemble mean at NGRIP, and overestimated at NEEM and WDC. At all sites, however, the reconstructed  $^{10}\text{Be}$  surface fluxes are within one standard deviation of the model ensemble mean, indicating that individual ensemble members match the reconstructed  $^{10}\text{Be}$  surface fluxes well. The fast decay phases at the NEEM and WDC sites are not reproduced by the model. A more detailed interpretation of the model results will be given in Section 7.

The magnitude of the simulated  $^{10}\text{Be}$  surface flux following the extreme 774 CE/775 SPE is comparable to that reported by Sukhodolov et al. (2017), who performed a similar study but with a focus on the impact of the 774 CE/775 SPE on stratospheric chemistry and nitrate deposition. Given that both model studies used different GLEs to estimate the intensity of the 774 CE/775 SPE (SOCOL: GLE05 from February 1956 and EMAC: GLE69 from January 2005), which differ in their intensity, derived enhancement factors and documentation by the worldwide neutron monitor systems, the overall agreement of both studies with the reconstructed  $^{10}\text{Be}$  surface fluxes is quite good. However, the model studies differ in other aspects, for example, the implementation of deposition processes, which justifies a further investigation of the topic.

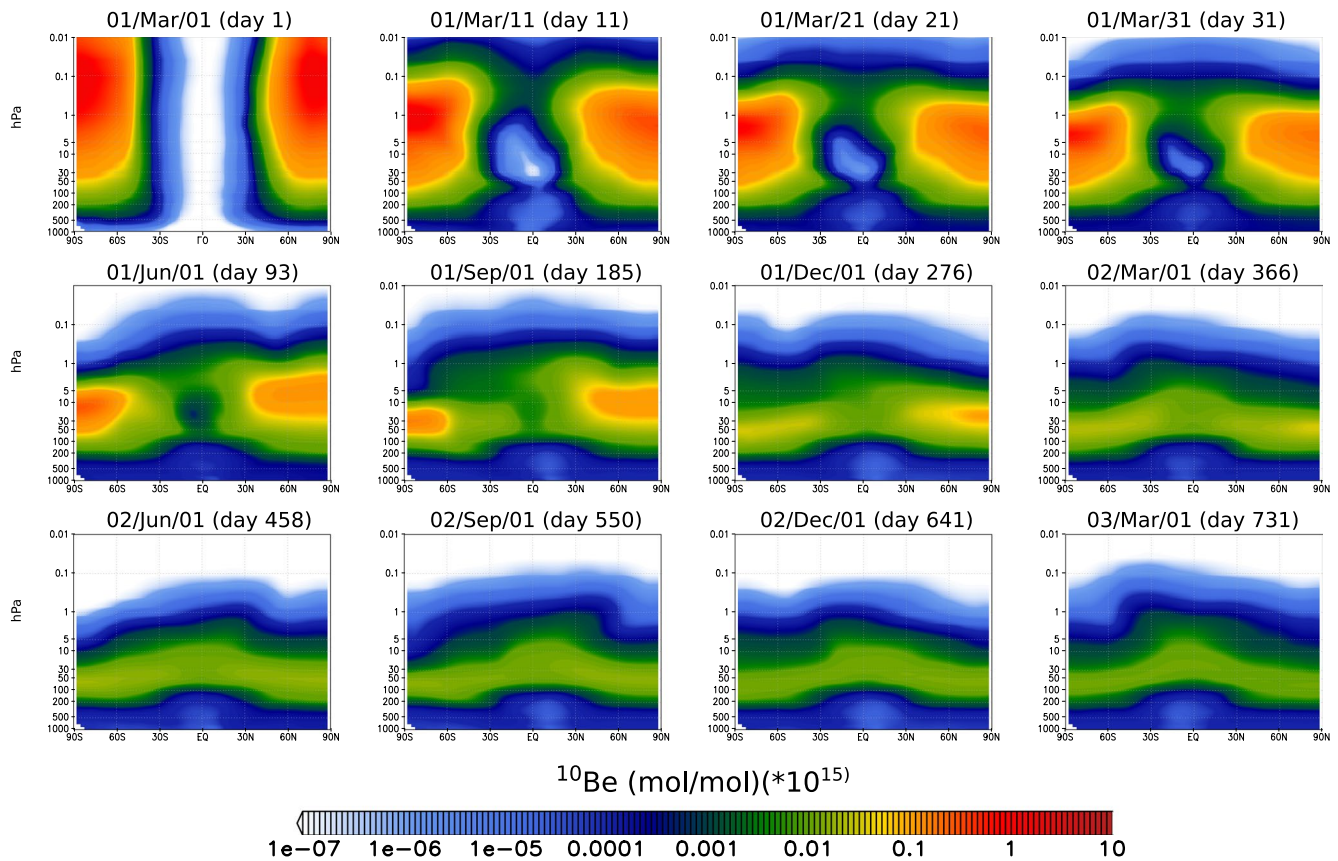


**Figure 4.** Long-term evolution of the daily mean  $^{10}\text{Be}$  mixing ratio [mol/mol] as a function of latitude and height at different times (YY/Mon/DD) after the tracer injection (day xyz). (top row) every 10 days of the first month, (middle row) every 3 months in the first year after the injection, and (bottom row) in the second year. Depicted is the ensemble mean over the March injection experiments.

### 3. Global Transport of $^{10}\text{Be}$

In the following, we focus on the subsequent global transport of the  $^{10}\text{Be}$  atoms after their production in the high latitude stratosphere. Figure 4 shows the temporal evolution of the 10-ensemble mean  $^{10}\text{Be}$  MR as a function of latitude and height at different times after the tracer injection in March: every 10 days of the first month (top row), every 3 months in the first year (middle row) and in the second year (bottom row). During an initial period, rapid latitudinal mixing takes place in the upper stratosphere and mesosphere, which is slightly more effective in the Northern Hemisphere (NH) due to enhanced planetary-scale mixing in the boreal late winter season (top row in Figure 4). Sedimentation leads to a gradual downward shift of the  $^{10}\text{Be}$  MR polar maxima to the middle stratosphere within 1 month and nearly complete removal of the  $^{10}\text{Be}$  mass from the mesosphere in the first year. In the tropical lower stratosphere, low values of  $^{10}\text{Be}$  MR are maintained throughout the first month after the tracer injection due to reduced meridional transport and mixing in this region, consistent with the tropical pipe model (Plumb, 1996) that shows the isolation of tropical air from middle latitudes. The  $^{10}\text{Be}$  particles that are produced directly in the upper troposphere are efficiently redistributed mainly by synoptic weather systems or the Hadley circulation in the troposphere. After about 1 month, a homogeneous distribution of low  $^{10}\text{Be}$  MR values has been established in the troposphere. The buildup of a sharp vertical gradient in  $^{10}\text{Be}$  MR around 100 hPa indicates that the tropopause acts as a barrier between the stratosphere and troposphere impeding an effective and fast downward transport of  $^{10}\text{Be}$ .

Following the initial mixing processes after the tracer injection, the  $^{10}\text{Be}$  transport is determined by the seasonal evolution of the BDC in the middle atmosphere. The BDC describes the net transport of air mass in the middle atmosphere, that is, the region between the tropopause and the mesopause at about 90 km altitude (e.g., Oberländer-Hayn et al., 2015). It consists of two components, a mean meridional circulation (MMC), characterized by the Transformed Eulerian mean (TEM) meridional and vertical residual velocities ( $\overline{v}^*$ ,  $\overline{w}^*$ ), and horizontal



mixing of air (Andrews et al., 1987). Both parts are induced dynamically by wave disturbances propagating upward from the troposphere in the winter and spring seasons. The amplitudes of the waves, predominantly large-scale planetary waves, grow with height and break in the stratosphere, thereby inducing an MMC with poleward downward transport in the winter stratosphere and upward transport in the tropics and summer hemisphere. Although being a zonal-mean diagnostic, the MMC results from 3-dimensional dynamical processes. Different planetary wave generation in the NH and Southern Hemisphere (SH) troposphere ultimately leads to stronger transport by the MMC in northern winter and spring compared to the corresponding southern season. Figure 4 (middle row) shows the sinking of the  $^{10}\text{Be}$  MR maximum to the lower stratosphere in winter polar regions (between day 93 and day 185 in the SH and between day 185 and day 366 in the NH). In the second year (Figure 4, bottom row), the stratospheric and tropospheric air masses are both well mixed, separated by a sharp vertical  $^{10}\text{Be}$  MR gradient at the tropopause. Figure 4 shows that the lower stratosphere (up to  $\sim 30$  km) acts as a  $^{10}\text{Be}$  reservoir preserving maximum  $^{10}\text{Be}$  abundances globally by nearly 2 years. This is consistent with earlier studies which found stratospheric lifetimes of aerosol-borne radionuclides in the order of one to 2 years (e.g., Feely et al., 1966).

#### 4. Stratosphere-to-Troposphere Pathways of $^{10}\text{Be}$

In this section, we examine in more detail the pathways of the  $^{10}\text{Be}$  atoms across the tropopause and in the troposphere. Figure 5 shows standardized (multi-year mean) monthly anomalies (z-scores) of the zonal mean  $^{10}\text{Be}$  MR for the lower stratosphere and the troposphere (at altitudes  $<30$  km, or pressure  $>10$  hPa). The standardized monthly anomalies have been calculated by subtracting the annual mean from the respective multi-annual monthly mean and dividing it by the standard deviation. Results are shown for the March injection experiments as an example, as the multi-year mean  $^{10}\text{Be}$  anomaly patterns and transport characteristics are not affected by the injection timing.

Above the tropopause (green line in Figure 5) black arrows indicate the intensity and direction of the stratospheric MMC, while in the troposphere the arrows illustrate the tropical Hadley cell with upwelling in the tropics and downwelling in the subtropics, and a year-round poleward-downward circulation cell in mid-to-high latitudes driven by synoptic wave activity (Plumb, 2002). Throughout the NH cold season (October to March), a quasi-hemispheric, positive  $^{10}\text{Be}$  anomaly slowly descends from the middle to the lower stratosphere, where anomalous  $^{10}\text{Be}$  atoms accumulate in April after continuous supply from above. The downward movement of the  $^{10}\text{Be}$  abundances is accomplished by the downward branch of the MMC in the high latitude winter stratosphere. A similar evolution is found in the SH stratosphere, where positive  $^{10}\text{Be}$  anomalies move downward from the middle to the lowermost stratosphere between early winter and spring (May to October). In contrast to the NH, the positive  $^{10}\text{Be}$  anomalies are found only in polar latitudes, as the sinking of polar air masses in Antarctic winter is confined to the stable SH polar vortices. Due to the generally weaker vertical residual velocity in the SH, the downward progression is slower than in Northern winter/spring. In the SH, the maximum positive anomalies reach the polar tropopause not until December, that is, in SH summer, about 2 months later compared to the respective NH spring season.

Exchange of air masses between the stratosphere and troposphere, that is, STE, occurs via both large-scale subsidence within the polar branch of the MMC and smaller-scale processes such as tropopause folds (Holton et al., 1995; Stohl et al., 2003). Transport of stratospheric air into the troposphere has been observed in the vicinity of the polar and subtropical jets, in cutoff lows, in mesoscale convective complexes, and associated with breaking gravity waves (Stohl et al., 2003 and references therein). A total of 50%–70% of the STE mass flux in the subtropics can be attributed to tropopause folds (Sprenger et al., 2003). Cross-tropopause transport has been studied intensively for ozone (e.g., Appenzeller et al., 1996; Hegglin & Shepherd, 2009; Holton et al., 1995; Meul et al., 2018) and  $^7\text{Be}$  (Liu et al., 2016).

To identify the contribution of tropopause folds to the  $^{10}\text{Be}$  STE in our simulations, we used the analysis software provided by Škerlak et al. (2015) and calculated the occurrence frequencies of tropopause folds based on the 100 model years. There is good agreement in the simulated seasonal and geographical distribution of the different tropopause fold types (shallow, medium, and deep) with the global climatology from ERA-Interim reanalyses (Škerlak et al., 2015) (not shown). The lower parts of the 12 panels in Figure 5 show latitudinal variations of the total tropopause fold frequencies for each month. It is found that most tropopause folds in the NH extratropics

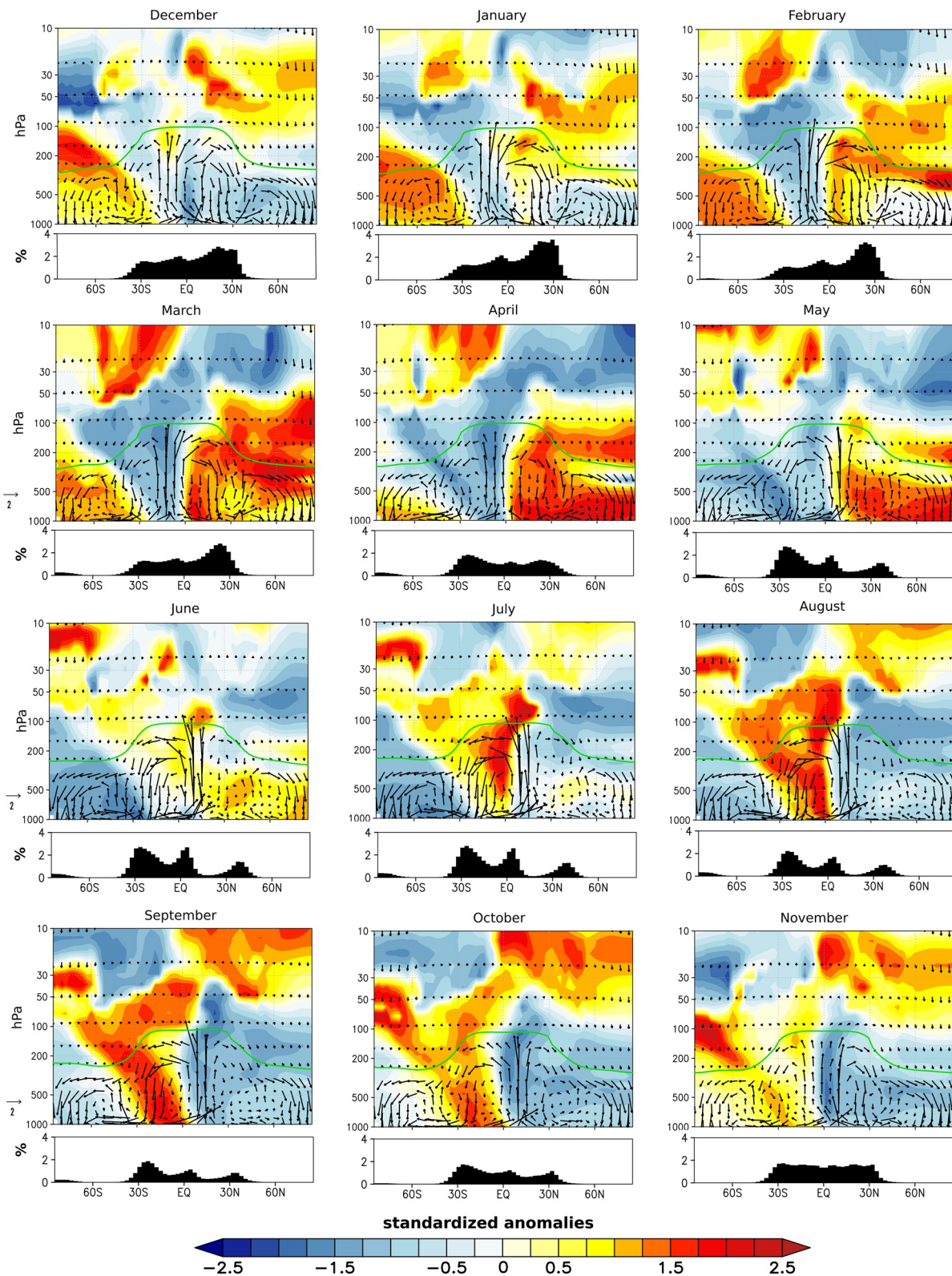


**Figure 5.** Monthly transport of  $^{10}\text{Be}$  between the middle stratosphere and the troposphere. Standardized anomalies of the multi-year monthly climatology of the  $^{10}\text{Be}$  MR (color shaded) from the annual mean for the March experiment. Black arrows denote the monthly climatology of the mean meridional circulation (The black arrow at the bottom left corner represents a mean meridional velocity of 2 m/s). The dynamical tropopause is shown as green line. The panels below show the zonal-mean distribution of the tropopause folding frequencies (%).

occur in winter and spring, with maxima between January and March. Hence, the positive  $^{10}\text{Be}$  anomalies reach the NH lower stratosphere during the season of high activity of tropopause folds. As a result, the accumulating lower stratospheric  $^{10}\text{Be}$  abundances are effectively transported by tropopause folds into the subtropical troposphere, from where they are further distributed toward the polar region between February and May (Figure 5). Thus, the downward transport of  $^{10}\text{Be}$  in the winter stratosphere by the BDC, followed by the  $^{10}\text{Be}$  import into the troposphere via tropopause folds and its meridional displacement by the tropospheric circulation turns out to be the dominant downward pathway of  $^{10}\text{Be}$  in the NH extratropics.

In the SH, the extratropical tropopause fold occurrence frequency maximizes in winter from May to July. In this period, however, no substantial  $^{10}\text{Be}$  enhancements exist in the SH lower stratosphere, and there is no effective downward displacement of  $^{10}\text{Be}$  into the troposphere through tropopause folds, except for August, where some positive stratospheric  $^{10}\text{Be}$  anomalies appear in the tropical lower troposphere. The transport of the SH high latitude  $^{10}\text{Be}$  anomalies into the troposphere is rather controlled by the MMC. After the positive  $^{10}\text{Be}$  anomalies have reached the lower stratosphere in early summer (December), they are further transported downward by the residual vertical velocity associated with the MMC in the lower stratosphere and synoptic weather systems in the troposphere, reaching the mid troposphere in February.

Figure 6 shows the temporal evolution of the ensemble mean daily and zonally averaged  $^{10}\text{Be}$  MR in the lower stratosphere at 74 hPa (Figure 6a), and the middle troposphere at 544 hPa (Figure 6b), as well as the  $^{10}\text{Be}$  surface flux (Figure 6c) for the full length of the model integrations (10 years).

After the injection, the highest levels of  $^{10}\text{Be}$  MR appear at mid to high latitudes of the lower stratosphere (74 hPa), while the  $^{10}\text{Be}$  MR remains low in the tropics (Figure 6a). Maximum  $^{10}\text{Be}$  MR is reached at NH high latitudes in February/March and at SH high latitudes in October/November, consistent with Figure 5. High  $^{10}\text{Be}$  MR values are well maintained in the first two simulation years and slowly decay afterward toward the end of the simulations. In the middle troposphere (544 hPa, Figure 6b), high  $^{10}\text{Be}$  values spread toward the tropics in both hemispheres (NH: March/April; SH: July to September) due to STE in tropopause folds and downward transport in the Hadley cell (see also Figure 5). The polar  $^{10}\text{Be}$  MR maxima in the mid troposphere are delayed by about 2 months compared to the lower stratosphere in both hemispheres. The latitudinal and seasonal patterns of the  $^{10}\text{Be}$  MR in the mid troposphere are no longer evident in the  $^{10}\text{Be}$  surface flux (Figure 6c), which is characterized by three latitudinal bands with high  $^{10}\text{Be}$  surface flux values, centered in NH mid latitudes, the tropics, and SH mid latitudes, with a pronounced annual cycle.

## 5. Simulated $^{10}\text{Be}$ Surface Flux

The  $^{10}\text{Be}$  surface flux distribution described in the previous section is the result of the different deposition processes that affect the  $^{10}\text{Be}$  atoms on their way through the troposphere down to the surface. Figure 7 displays the individual contributions of the deposition processes considered in the model simulations, to the total  $^{10}\text{Be}$  surface flux: the wet deposition flux (Figure 7a), the dry deposition flux (Figure 7c), and the sedimentation flux (Figure 7d). In addition, the summed precipitation from large-scale and convective processes, and snow fall is presented in Figure 7b. It is evident that wet deposition of  $^{10}\text{Be}$  atoms, that is, the washout and deposition of  $^{10}\text{Be}$  particles by precipitation, dominates the magnitude and geographical distribution of the  $^{10}\text{Be}$  surface flux. In the tropics,  $^{10}\text{Be}$  surface flux maxima follow closely the annual cycle of precipitation maxima associated with the Intertropical Convergence Zone and are thus out of phase by 6 months north and south of the Equator. Dry deposition at the surface has a minor effect when precipitation is strong, as most of the  $^{10}\text{Be}$  particles are removed by rainfall. In NH mid latitudes, we find a shift between the peak precipitation in the winter season and the strongest wet deposition flux in spring, which can be explained by the higher abundance of  $^{10}\text{Be}$  particles to be washed out in the troposphere as a result of more effective STE in spring. In the SH mid latitudes, the annual cycle in precipitation and wet deposition is less pronounced than in the NH. The  $^{10}\text{Be}$  surface flux generally decreases toward the polar regions. In the Arctic, the tropospheric  $^{10}\text{Be}$  abundance maximizes in spring, when precipitation is low compared to late summer/autumn. As a result, wet deposition is most efficient in the summertime. In the Antarctic, the strongest  $^{10}\text{Be}$  surface flux and wet deposition occur in March, when  $^{10}\text{Be}$  abundances are still high and precipitation starts to increase.

While the overall structure of the  $^{10}\text{Be}$  surface flux is determined by wet deposition, dry deposition at the surface contributes particularly in the mid latitudes of both hemispheres. The intensity of dry deposition is strongly

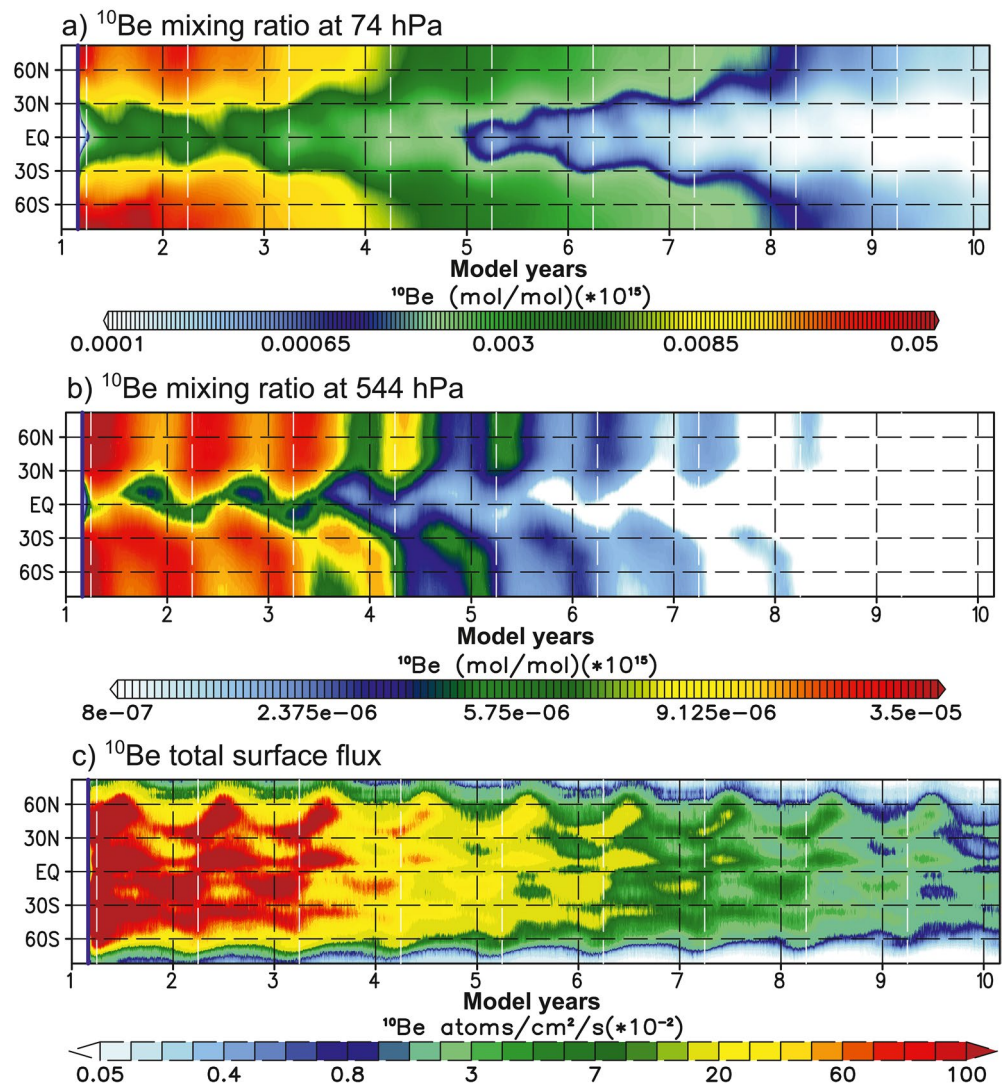


**Figure 6.** Temporal evolution of the  $^{10}\text{Be}$  mixing ratio (MR) in (a) the lower stratosphere (at 74 hPa) and (b) the middle troposphere (at 544 hPa), and (c) the  $^{10}\text{Be}$  total surface flux. The total surface flux includes dry and wet deposition and sedimentation. The blue vertical line indicates the timing of the injection, black and white dashed lines show each first of January and April, respectively. The time series is given in daily mean, zonal mean values for the ensemble mean with a  $^{10}\text{Be}$  injection in March.

controlled by the roughness length of the surface, which modulates surface friction and thus near-surface turbulence and quasi-boundary layer resistance. In months with active vegetation, that is, areas with large leaf canopy, the roughness length increases, and dry deposition intensifies. Although the mid latitude  $^{10}\text{Be}$  MR starts to decline in the free troposphere after May (Figure 6b), the Leaf Area Index (LAI) as a metric for active vegetation increases until July (not shown), and causes a shift of the  $^{10}\text{Be}$  dry deposition surface flux in NH mid latitudes to mid-summer (Figure 7c).

In the NH, the maximum dry deposition migrates north- and southward with the growing season, while it is more uniform throughout the year in the SH due to the predominance of the ocean surface. Sedimentation due to gravitational settling plays only a minor role in the  $^{10}\text{Be}$  surface flux in the first half simulation year.

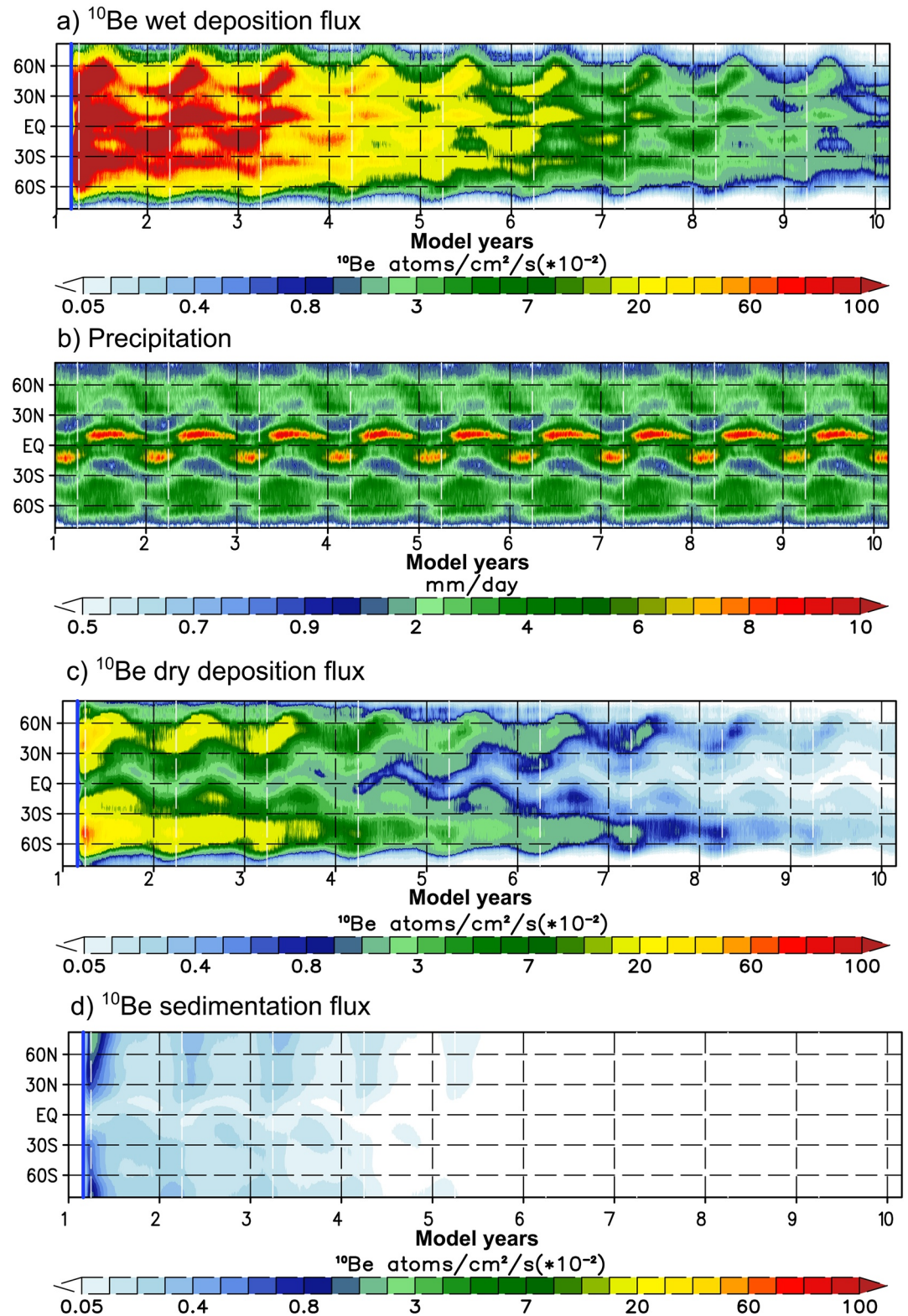


**Figure 7.** Temporal evolution of the  $^{10}\text{Be}$  surface flux (atoms/cm<sup>2</sup>/s) (a) due to wet deposition, (c) dry deposition, and (d) sedimentation. (b) total precipitation (mm/d). The blue vertical line indicates the timing of the injection, black and white dashed lines show each first of January and April, respectively. The time series are given in daily mean, zonal mean values for the ensemble mean with a  $^{10}\text{Be}$  injection in March.

## 6. Comparison With Reconstructed $^{10}\text{Be}$ Surface Fluxes

Based on the previous analysis of the pathways of the injected  $^{10}\text{Be}$  from the middle atmosphere down to the surface, we now interpret the differences between the reconstructed  $^{10}\text{Be}$  surface fluxes at the four drilling sites and provide supporting information on the seasonal variation in  $^{10}\text{Be}$  surface fluxes for future seasonally resolved analyses of the proxy data. The  $^{10}\text{Be}$  surface fluxes found in the NH and SH polar regions are the lowest worldwide (Figure 6c). Whereas in the middle troposphere the maximum  $^{10}\text{Be}$  MR appears at high latitudes (Figure 6b), both wet and dry depositions in the polar regions are too weak for an accumulation of  $^{10}\text{Be}$  atoms at the surface comparable to lower latitudes, particularly in Antarctica (Figures 7b and 7c). In order to disentangle the relative roles of the mid-tropospheric  $^{10}\text{Be}$  input and the different deposition sinks to the  $^{10}\text{Be}$  surface flux at the ice core sites, Figure 8 shows the simulated climatological (average of model years 2–10) seasonal cycle of the total  $^{10}\text{Be}$  surface flux (solid black line), the wet and dry deposition fluxes (dotted and dashed black lines), the 544 hPa  $^{10}\text{Be}$  MR (red line), and the total precipitation (blue line). To account for the high local variability in precipitation, the model results represent an area-weighted average for each of the drilling sites NGRIP (76.7°N–71.1°N; 36.6°W–47.8°W), NEEM (79.5°N–73.9°N; 45°W–56.2°W), WDC (82.3°S–76.7°S; 106.9°W–118.1°W), and Dome Fuji (79.5°S–73.9°S; 33.8°E–45°E). For all sites, the absolute values of the seasonal cycle (Figure 8, left column) and its amplitude (the relative value) (Figure 8, right column) are shown. In Greenland (NGRIP, NEEM) the  $^{10}\text{Be}$  surface flux peaks in July, about 2 months later than the mid-tropospheric  $^{10}\text{Be}$  MR. This shift is caused by the increasing precipitation activity in early summer which leads to enhanced wet deposition of  $^{10}\text{Be}$  atoms, thus compensating for the already declining  $^{10}\text{Be}$  MR. In September, when precipitation reaches its maximum at both sites, a weak secondary enhancement of the  $^{10}\text{Be}$  surface flux develops, although the tropospheric  $^{10}\text{Be}$  input has declined over summer. At both Greenlandic sites, wet deposition contributes about 80–90% to the peak in total  $^{10}\text{Be}$  surface flux and determines both the annual cycle and the timing of the peak.

At the two Antarctic drilling sites, the  $^{10}\text{Be}$  surface flux peaks in February, although considerable differences in the magnitude of the  $^{10}\text{Be}$  surface flux are simulated between WDC and Dome Fuji. Although precipitation is moderate in the WDC area in SH summer, the February peak mainly results from wet deposition which leads to an effective washout of  $^{10}\text{Be}$  atoms at the time of maximum tropospheric  $^{10}\text{Be}$  MR. Similar to the Greenlandic sites, the precipitation peak in June generates a secondary maximum in the  $^{10}\text{Be}$  surface flux despite low  $^{10}\text{Be}$  MR. In the Dome Fuji area, the lowest  $^{10}\text{Be}$  surface flux of all sites is simulated, with about 25% of the  $^{10}\text{Be}$  surface flux at the WDC area in February. This timing matches the season of strongest  $^{10}\text{Be}$  MR abundance in the troposphere in contrast to the other sites; at Dome Fuji, the contribution of wet deposition to the  $^{10}\text{Be}$  total surface flux is negligible throughout the year and dry deposition is the dominant contributor to the  $^{10}\text{Be}$  surface flux.

To isolate the factors responsible for the different magnitude of the  $^{10}\text{Be}$  surface fluxes at the two Greenlandic and the two Antarctic drilling sites, Figure 9 shows the simulated ensemble mean annual mean precipitation and wet deposition ratio for Greenland and Antarctica. The respective locations of the four ice core drilling sites are indicated by white marks. The differing behavior can be explained by the local meteorological conditions at the individual drilling sites. In Greenland (Figure 9, top row), annual mean total precipitation is low in the northern and central parts of the ice shield and increases toward the south-east. While the NGRIP drilling site (white cross) is located in the dry center of Greenland at an elevation of 2,917 m above sea level, the NEEM drilling (white square) was carried out closer to the west coast in a warmer region with a strong precipitation gradient. Hence, wet deposition has a smaller effect on the climatological annual mean total  $^{10}\text{Be}$  surface flux at NGRIP (10%) than at NEEM, where a wet deposition ratio of 60–70% largely explains the fast increasing and high  $^{10}\text{Be}$  surface flux in summer (see Figure 9, right panels).

The Dome Fuji site (white triangle in Figure 9, bottom row) is located on the central Antarctic ice shield at an elevation of 3,810 m above sea level. The EMAC model simulates very low precipitation of less than 0.1 mm/d at Dome Fuji (Figure 9, bottom left), in good agreement with ERA-Interim reanalyses (not shown). In such dry climate conditions, the accumulation of  $^{10}\text{Be}$  atoms by snow fall becomes insignificant. The contribution of wet deposition to the total  $^{10}\text{Be}$  surface flux at Dome Fuji is less than 10% (Figure 9, bottom right). Actually, Figure 8 shows that dry deposition exceeds wet deposition at the Dome Fuji site, in good agreement with model simulations by Field et al. (2006) and Heikkilä et al. (2013). The low contribution of wet deposition explains the weak response of the  $^{10}\text{Be}$  surface flux and the slow decay after the peak year, which is well reproduced by the model. In contrast, at the WDC drilling site, located in western Antarctica at a lower elevation, snow accumulation

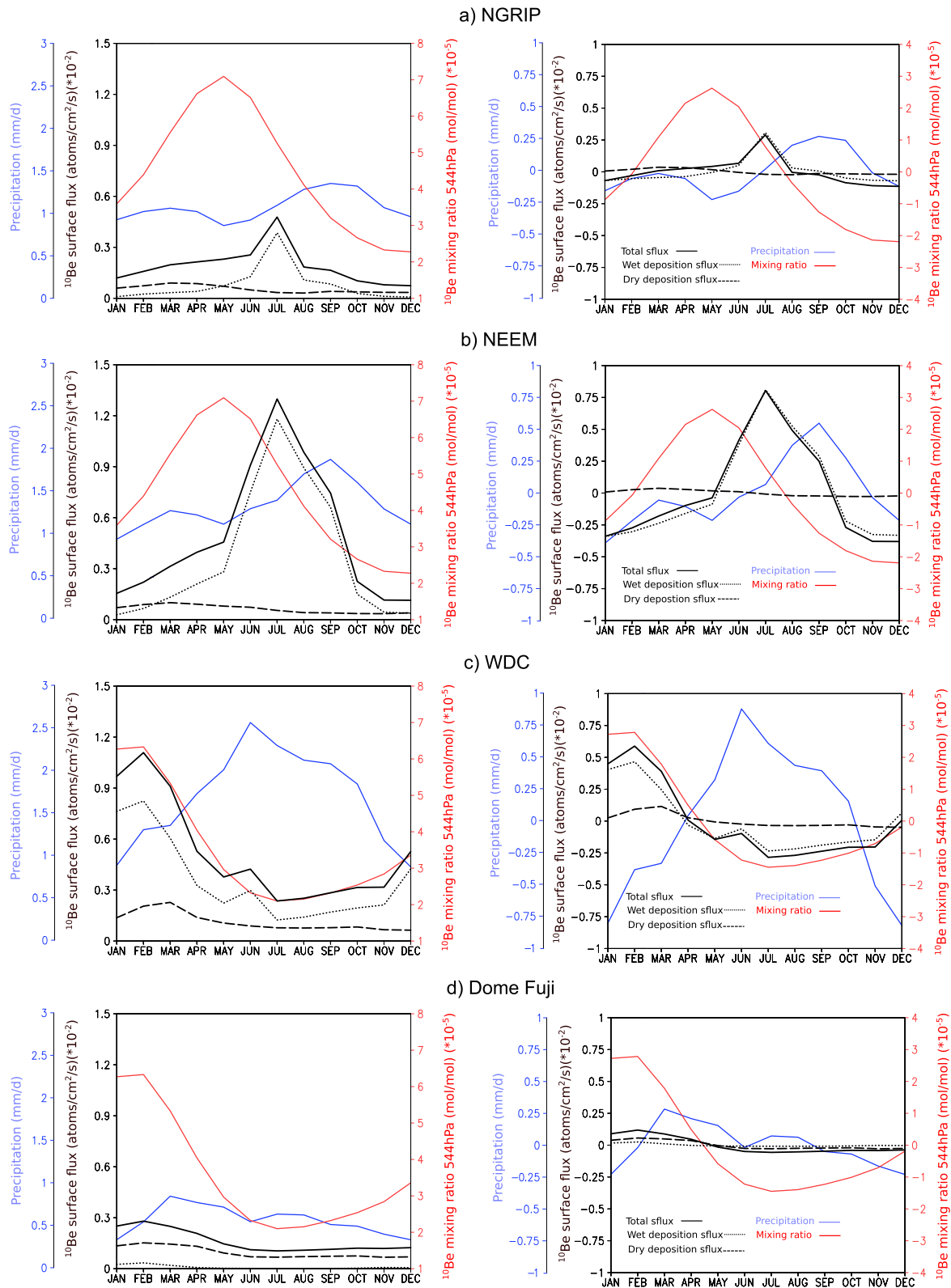
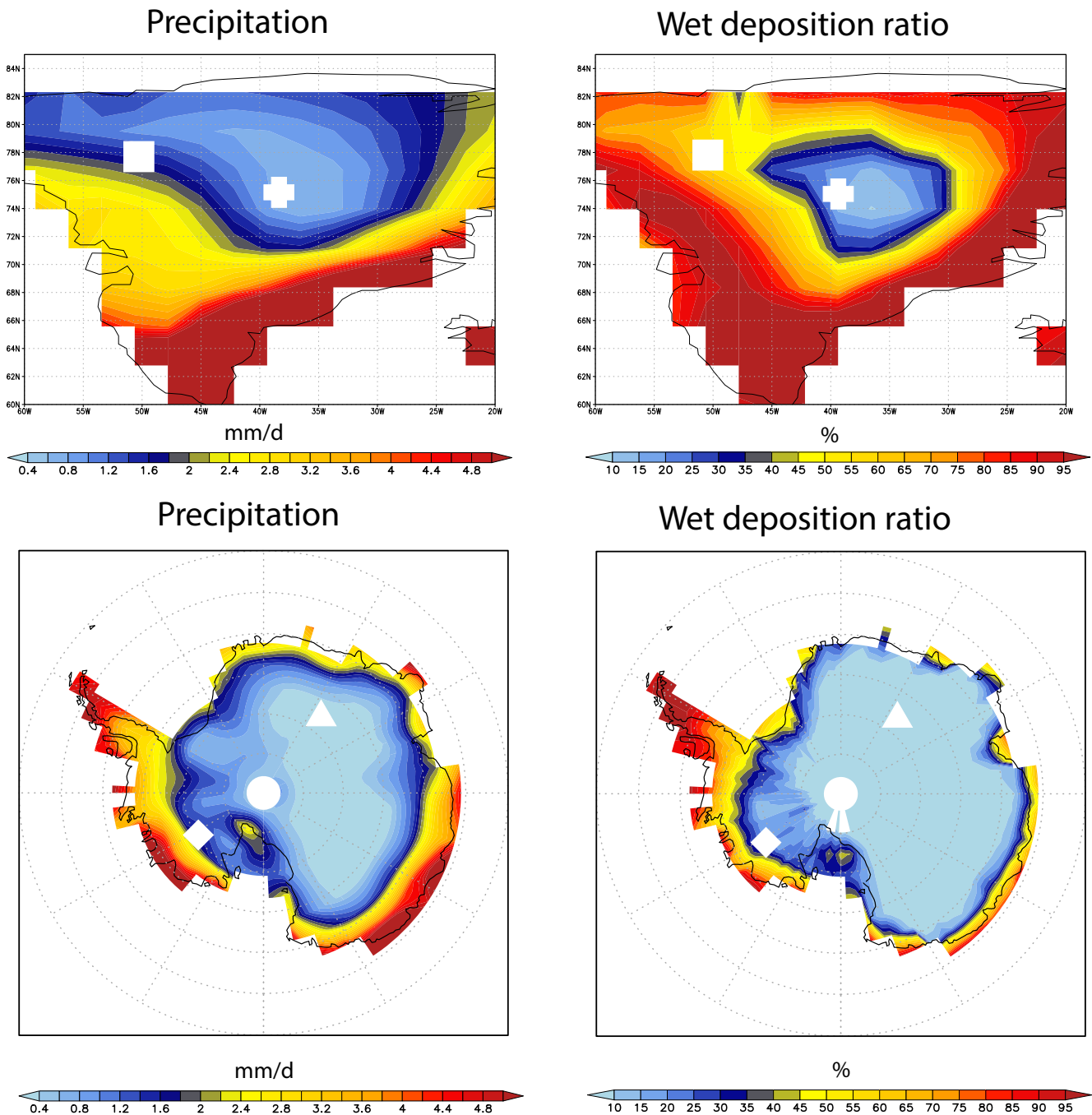


Figure 8.



**Figure 9.** Simulated annual mean total precipitation (mm/d) and ratio of wet deposition flux to total  $^{10}\text{Be}$  surface flux (%) for Greenland (top panels) and Antarctica (bottom panels). Also included are the locations of the Greenlandic drilling sites North Greenland Ice core Project (white cross) and North Greenland Eemian Ice Drilling (white square), and the Antarctic drilling sites West Antarctic Ice Sheet Divide Core (white diamond) and Dome Fuji (white triangle).

**Figure 8.** Seasonal variation of the climatological total  $^{10}\text{Be}$  surface flux (solid black line), the  $^{10}\text{Be}$  surface flux by wet deposition (black dotted line), the  $^{10}\text{Be}$  surface flux by dry deposition (black dashed line), and the total precipitation (blue line) for four regions representing the drilling sites (a) North Greenland Ice core Project (NGRIP), (b) North Greenland Eemian Ice Drilling (NEEM), (c) West Antarctic Ice Sheet Divide Core (WDC), and (d) Dome Fuji. Also included is the zonal mean  $^{10}\text{Be}$  MR at 544 hPa for  $70^{\circ}\text{--}80^{\circ}\text{N}$  (NGRIP, NEEM) and  $70^{\circ}\text{--}80^{\circ}\text{S}$  (WDC, Dome Fuji) (red line). The left column displays absolute values, and the right column the amplitude (the relative values) of the annual cycle.



rates are higher due to the proximity of the drilling site to the region of main cyclone density around Antarctica associated with the Amundsen-Bellinghousen Seas Low (e.g., Fogt et al., 2012). Hence, wet deposition has a stronger effect on the  $^{10}\text{Be}$  surface flux leading to higher values at WDC than at Dome Fuji.

The model generally captures the reconstructed  $^{10}\text{Be}$  surface fluxes well for the drilling sites with the low influence of wet deposition (NGRIP and Dome Fuji), while it seems to overestimate the peak of the reconstructed  $^{10}\text{Be}$  surface flux at the sites with the higher impact of synoptic weather systems and precipitation, such as NEEM and WDC (Figure 3). This might be due to uncertainty in the simulated precipitation amount and/or in the model parameterizations for aerosol wet removal. On the other side, Figure 3 shows that the variability of the  $^{10}\text{Be}$  surface flux within the model ensemble is considerably larger for the NEEM and WDC sites which are more strongly influenced by synoptic weather variability than for the drier sites. For both sites, the reconstructed  $^{10}\text{Be}$  surface flux matches the one sigma standard deviation derived from the model ensemble. This implies that the magnitude of the reconstructed  $^{10}\text{Be}$  surface flux at NEEM and WDC might also be the result of a year with specific meteorological conditions in the NH at these sites.

As a result of the differential meteorological impact at the drilling sites, a negative gradient of the  $^{10}\text{Be}$  surface flux from near-coastal to central drilling sites is evident in both the annual mean of the reconstructed peak year and of the model ensemble mean for the Antarctic drilling sites (Figure 3). In contrast, the reconstructed  $^{10}\text{Be}$  surface fluxes in Greenland do not display the negative coast-to-central gradient in  $^{10}\text{Be}$  surface flux, while the model shows the expected behavior. We therefore assume that the year of the 774/775 AD SPE was shaped by specific meteorological conditions in the NH, which interfered with the climatological situation. Weather in Greenland is strongly influenced by the North Atlantic Oscillation (NAO) which is characterized by large interannual variability. A positive NAO phase would be associated with low precipitation anomalies in west Greenland and high anomalies in east Greenland (e.g., Björk et al., 2018; Wong et al., 2015) and support a  $^{10}\text{Be}$  surface flux pattern as found in the reconstructions for NGRIP and NEEM. A recent reconstruction of the NAO timeseries over the last two millennia indeed shows, that the year 774/775 AD lies within a period with a clear tendency toward a positive NAO (Hernández et al., 2020). This is in agreement with the lack of a clear gradient in the reconstructed total surface flux between the NEEM and NGRIP drilling site.

## 7. Concluding Remarks

By combining the state-of-the-art climate model EMAC with the operational SEP warning system WASAVIES to estimate the initial yield of  $^{10}\text{Be}$ , an improved representation of both the initial concentration of  $^{10}\text{Be}$  and its atmospheric transport and surface deposition was achieved. Using the new model setup, we simulated the transport, mixing, and deposition of  $^{10}\text{Be}$  produced by the extreme SPE of 774 CE/775 under preindustrial boundary conditions. With the aid of a 3-dimensional model, covering the full stratosphere and mesosphere (up to  $\sim 80$  km height), a realistic representation of the  $^{10}\text{Be}$  transport by the major stratospheric circulation system, the BDC, including its upper stratosphere and mesosphere branches, is achieved. The model thus considers implicitly the effects of 3-dimensional planetary wave activity on the global circulation and mass transport. The role of STE as well as the relative contributions of the different deposition processes (dry, wet, and sedimentation) to the  $^{10}\text{Be}$  surface fluxes have been examined. To evaluate the new model setup, we compared the simulated  $^{10}\text{Be}$  surface flux to the latest estimates based on ice core reconstructions from Greenland and Antarctica.

Our results show a fast horizontal mixing of the produced  $^{10}\text{Be}$  particles with lower latitude air in both the stratosphere and the troposphere. Sedimentation leads to gradual removal of the aerosol-borne  $^{10}\text{Be}$  atoms in the mesosphere. Following the initial mixing processes, the  $^{10}\text{Be}$  transport is determined by the seasonal evolution of the BDC with a downward displacement of the  $^{10}\text{Be}$  MR to the polar lower stratosphere in winter and spring of each hemisphere, where it accumulates until April in the NH and December in the SH. The weaker downwelling in the SH winter stratosphere leads to a hemispheric shift in the timing of the maximum  $^{10}\text{Be}$  concentration in the lower stratosphere by about 2 months from spring in the NH to summer in the SH.

We further found distinct hemispheric differences in the cross-tropopause transport of the lower stratospheric  $^{10}\text{Be}$  abundances into the troposphere. In our simulations, the high  $^{10}\text{Be}$  concentrations in the lower stratosphere during NH spring are effectively imported into the troposphere via tropopause folds in the NH extratropics, which occur predominantly in NH winter/spring between January and March. In contrast in the SH summer, when the  $^{10}\text{Be}$  concentrations reach their maximum in the lower stratosphere, tropopause folds play a less important role. As a result, the further

downward pathway of  $^{10}\text{Be}$  into the troposphere is dominated in the NH by the  $^{10}\text{Be}$  transport in tropopause folds and its subsequent meridional displacement by the tropospheric circulation, while in the SH large-scale downwelling of  $^{10}\text{Be}$  atoms into the high-latitude troposphere in summer dominates. This is consistent with a study exploring the transport pathways of  $^{10}\text{Be}$  to Antarctica (Pedro, Heikkilä, et al., 2011) and simulations using aerosols to track stratospheric air masses to Antarctica (e.g., Stohl & Sodemann, 2010). Due to the intensity of stratospheric downwelling and the STE mechanisms at work, our results show a shift in the maximum  $^{10}\text{Be}$  MR timing between the lower stratosphere and troposphere by about 1–2 months to May (NH) and February (SH) at 544 hPa.

In order to compare our simulated  $^{10}\text{Be}$  surface fluxes with the four ice core drilling sites, we examined in detail the mechanisms determining the deposition of  $^{10}\text{Be}$  atoms at the different sites. In both polar regions,  $^{10}\text{Be}$  surface fluxes maximize in the respective summer season (July in Greenland; February in Antarctica). The timing of the peak, however, results from different processes acting in the two hemispheres. The magnitude and seasonal timing of the  $^{10}\text{Be}$  surface fluxes are steered by the interplay between the available  $^{10}\text{Be}$  abundance in the mid-troposphere and the seasonal cycle of regional precipitation. According to our simulations, differences in this interplay between the Greenland and Antarctic sites, as well as between the two Antarctic sites are responsible for the range of reconstructed and simulated  $^{10}\text{Be}$  surface fluxes. At the Greenlandic drilling sites, the  $^{10}\text{Be}$  surface flux maximum in July is the result of optimal exploitation of available  $^{10}\text{Be}$  abundance in the troposphere (maximum in May) and precipitation intensity (maximum in September/October). Due to the dominant impact of wet deposition at both Greenlandic sites, this time shift leads to a lag of the  $^{10}\text{Be}$  surface flux maximum by 2 months compared to the  $^{10}\text{Be}$  abundance in the middle troposphere. In contrast, at the two Antarctic sites, maximum  $^{10}\text{Be}$  surface fluxes occur at the time of maximum tropospheric  $^{10}\text{Be}$  MR in January/February. No temporal shift occurs between the tropospheric  $^{10}\text{Be}$  MR maximum and the peak in  $^{10}\text{Be}$  surface fluxes, as at the time of the tropospheric  $^{10}\text{Be}$  maximum, precipitation and hence wet deposition are either moderate (at WDC) or negligible (at Dome Fuji). At WDC the moderate summer precipitation removes effectively the large supply of tropospheric  $^{10}\text{Be}$  in January/February before the precipitation maximum is reached in winter.

Although seasonally resolved ice core data analyses for the 774 CE/775 SPE are scheduled for the near future, they are not available yet. However, a qualitative comparison to more recent proxy analyses is possible. For instance, the timing of the highest values in the  $^{10}\text{Be}$  surface flux in our experiments at both Greenlandic drilling sites is comparable to seasonally resolved proxy analyses of  $^{10}\text{Be}$  accumulation from recent snow pit analyses at the NGRIP (Heikkilä, Beer, Jouzel, et al., 2008) (1986–1990) and at Dye3 (Beer et al., 1991) (1978–1983) drilling sites in central and southern Greenland. Both studies also report summer/fall maxima of the  $^{10}\text{Be}$  surface flux, however, find considerable variability in their measured  $^{10}\text{Be}$  timeseries with secondary maxima in spring. At the Antarctic sites, the maxima in the modeled  $^{10}\text{Be}$  surface flux are in line with  $^{10}\text{Be}$  snow pit analyses at the Dome Summit South (DSS) drilling site (1999–2009) from Law Dome, East Antarctica, which show maxima in  $^{10}\text{Be}$  between austral summer and fall (Pedro, Smith, et al., 2011).

The simulation of the reconstructed annual mean  $^{10}\text{Be}$  surface flux at the four drilling sites showed good agreement in the peak  $^{10}\text{Be}$  surface flux of the 774/775 AD SPE and the slow decay in the following 5 years between the EMAC ensemble mean and those sites that are located in central Greenland (NGRIP) or central Antarctica (Dome Fuji). Higher peak  $^{10}\text{Be}$  surface fluxes than in the reconstructions and a large spread within the simulation ensemble were simulated for the NEEM and WDC drilling sites which are located in more humid regions and more affected by tropospheric weather systems. These differences could be attributed to the relevance of wet deposition for  $^{10}\text{Be}$ . The model reproduces well the decrease in maximum  $^{10}\text{Be}$  surface flux from the moist coastal to the dry central sites, as reconstructed for the Antarctic sites WDC and Dome Fuji. In Greenland, this negative slope toward the more central NGRIP site is only found in the model, possibly indicating a positive anomaly in the NAO phase and associated dryer (wetter) conditions at NEEM (NGRIP) at the time of the SPE.

It finally has to be taken into account that our simulations assumed a preindustrial climate state (representative for the year 1850) which might differ from the actual state of the year 774 CE/775, with consequences for local meteorological parameters and dry and wet deposition. Moreover, a PI-climatology for SSTs has been prescribed which dampens the interannual variability in the troposphere with consequences for the spread in the modeled annual mean  $^{10}\text{Be}$  surface flux.

The model setup presented in this study allows for a multidisciplinary evaluation of solar-terrestrial data, state-of-the-art climate modeling, and geochronological reconstructions. It can easily be applied to other periods

with documented extreme events, such as the SPE in the tenth century. Seasonally resolved ice core data analysis will be incorporated, when available. In the next step, the model will be expanded by a parameterization of GCR-produced  $^{10}\text{Be}$  surface fluxes and a carbon cycle model to include the cosmogenic  $^{14}\text{C}$  radionuclide in future applications.

## Data Availability Statement

The model data for this research are not publicly available due to large storage space requirements. Data are stored at the HLRN supercomputing facility and will be made available upon reasonable request to the corresponding author. The proxy based reconstructions for the  $^{10}\text{Be}$  surface flux at the different drilling locations can be requested from the corresponding authors of the publications Miyake et al. (2015), Sigl et al. (2015), and Mekhaldi et al. (2015).

## Acknowledgments

The authors would like to acknowledge the Project for Solar Terrestrial Environment (PSTEP) for funding this project, Florian Mekhaldi for providing the surface flux data for the NGRIP, NEEM and WDC drilling sites, Astrid Kerkweg for giving advice regarding the dry deposition parameterization and the HLRN supercomputing facility in Berlin for the granted computing time. We would also like to thank Bojan Škerlak and colleagues for providing the tropopause folding frequency analysis software at <https://svn.iac.ethz.ch/websvn/pub/browse/tropofold.echam>. This work was supported partially by JSPS KAKENHI Grant 15H05816 and 17H01159. This work has also been inspired by the International Space Science Institute team, Solar Extreme Events: Setting Up a Paradigm (SEESUP). Open Access funding enabled and organized by Projekt DEAL.

## References

- Andrews, D. G., Holton, J. R., & Leovy, C. B. (1987). *Middle atmosphere dynamics* (p. 489). Academic Press.
- Appenzeller, C., Holton, J. R., & Rosenlof, K. H. (1996). Seasonal variation of mass transport across the tropopause. *Journal of Geophysical Research*, *101*(D10), 15071–15078. <https://doi.org/10.1029/96JD00821>
- Beer, J., Finkel, R. C., Bonani, G., Gäggeler, H., Görlach, U., & Jacob, P. (1991). Seasonal variations in the concentration of  $^{10}\text{Be}$ ,  $\text{Cl}^-$ ,  $\text{NO}_3^-$ ,  $\text{SO}_4^{2-}$ ,  $\text{H}_2\text{O}_2$ ,  $^{210}\text{Pb}$ ,  $^{210}\text{Po}$ , mineral dust, and  $\sigma^{18}\text{O}$  in Greenland snow. *Atmospheric Environment. Part A. General Topics*, *25*(5–6), 899–904. [https://doi.org/10.1016/0960-1686\(91\)90131-P](https://doi.org/10.1016/0960-1686(91)90131-P)
- Bieber, J. W., Clem, J., Evenson, P., Pyle, R., Sáiz, A., & Ruffolo, D. (2013). Giant ground level enhancement of relativistic solar protons on 2005 January 20. I. Spaceship Earth observations. *The Astrophysical Journal*, *771*(2), 92. <https://doi.org/10.1088/0004-637X/771/2/92>
- Björk, A. A., Aagaard, S., Lütt, A., Khan, S. A., Box, J. E., Kjeldsen, K. K., & Kjær, K. H. (2018). Changes in Greenland's peripheral glaciers linked to the North Atlantic Oscillation. *Nature Climate Change*, *8*(1), 48–52. <https://doi.org/10.1038/s41558-017-0029-1>
- Büntgen, U., Wacker, L., Galván, J. D., Arnold, S., Arseneault, D., Baillie, M., et al. (2018). Tree rings reveal globally coherent signature of cosmogenic radiocarbon events in 774 and 993 CE. *Nature Communications*, *9*(1), 1–7. 3605. <https://doi.org/10.1038/s41467-018-06036-0>
- Dietmüller, S., Jöckel, P., Tost, H., Kunze, M., Gellhorn, C., Brinkop, S., et al. (2016). A new radiation infrastructure for the Modular Earth Submodel System (MESSy, based on version 2.51). *Geoscientific Model Development*, *9*, 2209–2222. <https://doi.org/10.5194/gmd-9-2209-2016>
- Elsässer, C. (2013). Exploration of  $^{10}\text{Be}$  ice core records using a climatological model approach. *Cosmogenic production versus climate variability*, PhD thesis. University of Heidelberg. <https://doi.org/10.11588/heidok.00016349>
- Feely, H. W., Seitz, H., Lagomarsino, J., & Biscaye, P. E. (1966). Transport and fallout of stratospheric radioactive debris. *Tellus*, *18*, 316–328. <https://doi.org/10.3402/tellusa.v18i2-3.9619>
- Field, C., Schmidt, G., Koch, D., & Salyk, C. (2006). Modeling production and climate-related impacts on  $^{10}\text{Be}$  concentration in ice cores. *Journal of Geophysical Research*, *111*, D15107. <https://doi.org/10.1029/2005jd006410>
- Fogt, R. L., Vovrosh, A. J., Langen, R. A., & Simmonds, I. (2012). The characteristic variability and connection to the underlying synoptic activity of the Amundsen-Bellinghousen Seas Low. *Journal of Geophysical Research*, *117*, D07111. <https://doi.org/10.1029/2011JD017337>
- Foucart, Y., & Bonnel, B. (1980). Computations of solar heating of the Earth's atmosphere: A new parameterization. *Beiträge zur Physik der Atmosphäre*, *53*, 35–62.
- Ganzeveld, L., & Lelieveld, J. (1995). Dry deposition parameterization in a chemistry general circulation model and its influence on the distribution of reactive trace gases. *Journal of Geophysical Research*, *100*(D10), 20999–21012. <https://doi.org/10.1029/95JD02266>
- Ganzeveld, L., Lelieveld, J., & Roelofs, G. J. (1998). A dry deposition parameterization for sulfur oxides in a chemistry and general circulation model. *Journal of Geophysical Research*, *103*(D5), 5679–5694. <https://doi.org/10.1029/97JD03077>
- Giorgetta, M. A., & Bengtsson, L. (1999). Potential role of the quasi-biennial oscillation in the stratosphere-troposphere exchange as found in water vapor in general circulation model experiments. *Journal of Geophysical Research*, *104*, 6003–6019. <https://doi.org/10.1029/1998JD200112>
- Güttler, D., Adolphi, F., Beer, J., Bleicher, N., Boswijk, G., Christl, M., et al. (2015). Rapid increase in cosmogenic  $^{14}\text{C}$  in AD 775 measured in New Zealand kauri trees indicates short-lived increase in  $^{14}\text{C}$  production spanning both hemispheres. *Earth and Planetary Science Letters*, *411*, 290–297. <https://doi.org/10.1016/j.epsl.2014.11.048>
- Hambaryan, V., & Neuhäuser, R. A. (2013). Galactic short gamma-ray burst as cause for the  $^{14}\text{C}$  peak in AD 774/5. *Monthly Notices of the Royal Astronomical Society*, *430*, 32–36. <https://doi.org/10.1093/mnras/sts378>
- Hegglin, M. I., & Shepherd, T. G. (2009). Large climate-induced changes in ultraviolet index and stratosphere-to-troposphere ozone flux. *Nature Geoscience*, *2*(10), 687–691. <https://doi.org/10.1038/NGEO604>
- Heikkilä, U., Beer, J., Abreu, J. A., & Steinhilber, F. (2013). On the atmospheric transport and deposition of the cosmogenic radionuclides ( $^{10}\text{Be}$ ): A review. *Space Science Reviews*, *176*, 321–332. <https://doi.org/10.1007/s11214-011-9838-0>
- Heikkilä, U., Beer, J., & Alfimov, V. (2008). Beryllium-10 and beryllium-7 in precipitation in Dübendorf (440 m) and at Jungfraujoch (3580 m), Switzerland (1998–2005). *Journal of Geophysical Research*, *113*(D11), D11104. <https://doi.org/10.1029/2007JD009160>
- Heikkilä, U., Beer, J., Jouzel, J., Feichter, J., & Kubik, P. (2008).  $^{10}\text{Be}$  measured in a GRIP snow pit and modeled using the ECHAM5-HAM general circulation model. *Geophysical research letters*, *35*(5), L05817. <https://doi.org/10.1029/2007GL033067>
- Hernández, A., Sánchez-López, G., Pla-Rabes, S., Comas-Bru, L., Parnell, A., Cahill, N., & Giral, S. (2020). A 2,000-year Bayesian NAO reconstruction from the Iberian Peninsula. *Scientific reports*, *10*(1), 1–15. <https://doi.org/10.1038/s41598-020-71372-5>
- Holton, J. R., Haynes, P. H., McIntyre, M. E., Douglass, A. R., Rood, R. B., & Pfister, L. (1995). Stratosphere-troposphere exchange. *Reviews of Geophysics*, *33*(4), 403–439. <https://doi.org/10.1029/95RG02097>
- Jöckel, P., Kerkweg, A., Pozzer, A., Sander, R., Tost, H., Riede, H., et al. (2010). Development cycle 2 of the modular Earth submodel system (MESSy2). *Geoscientific Model Development*, *3*, 717–752. <https://doi.org/10.5194/gmd-3-717-2010>
- Jöckel, P., Tost, H., Pozzer, A., Kunze, M., Kirner, O., Brenninkmeijer, C. A., et al. (2016). Earth system chemistry integrated modeling (ESCI-Mo) with the modular Earth submodel system (MESSy) version 2.51. *Geoscientific Model Development*, *9*(3), 1153–1200. <https://doi.org/10.5194/gmd-9-1153-2016>

- Junge, C. E. (1963). *Air chemistry and Radioactivity*. (Vol. 4) International Geophysics Series, Academic Press.
- Kerkweg, A., Buchholz, J., Ganzeveld, L., Pozzer, A., Tost, H., & Jöckel, P. (2006). An implementation of the dry removal processes DRY DEPosition and SEDImentation in the Modular Earth Submodel System (MESSy). *Atmospheric Chemistry and Physics*, 6(12), 4617–4632. <https://doi.org/10.5194/acp-6-4617-2006>
- Koch, D., & Rind, D. (1998). Beryllium 10/beryllium 7 as a tracer of stratospheric transport. *Journal of Geophysical Research*, 103, 3907–3917. <https://doi.org/10.1029/97JD03117>
- Kunze, M., Godolt, M., Langematz, U., Grenfell, J. L., Hamann-Reinus, A., & Rauer, H. (2014). Investigating the early Earth faint young Sun problem with a general circulation model. *Planetary and Space Science*, 98, 77–92. <https://doi.org/10.1016/j.pss.2013.09.011>
- Lifton, N., Sato, T., & Dunai, T. J. (2014). Scaling in situ cosmogenic nuclide production rates using analytical approximations to atmospheric cosmic-ray fluxes. *Earth and Planetary Science Letters*, 386, 149–160. <https://doi.org/10.1016/j.epsl.2013.10.052>
- Liu, H., Considine, D. B., Horowitz, L. W., Crawford, J. H., Rodriguez, J. M., Strahan, S. E., & Yantosca, R. M. (2016). Using beryllium-7 to assess cross-tropopause transport in global models. *Atmospheric Chemistry and Physics*, 16(7), 4641–4659. <https://doi.org/10.5194/acp-16-4641-2016>
- Liu, Y., Zhang, Z.-F., Ling, M.-X., Shen, C.-C., Liu, W.-G., Sun, X.-C., et al. (2014). Mysterious abrupt carbon-14 increase in coral contributed by a comet. *Scientific Reports*, 4, 3728. <https://doi.org/10.1038/srep03728>
- Malinina, E., Rozanov, A., Rozanov, V., Liebing, P., Bovensmann, H., & Burrows, J. P. (2018). Aerosol particle size distribution in the stratosphere retrieved from SCIAMACHY limb measurements. *Atmospheric Measurement Techniques*, 11, 2085–2100. <https://doi.org/10.5194/amt-11-2085-2018>
- Masarik, J., & Beer, J. (1999). Simulation of particle fluxes and cosmogenic nuclide production in the Earth's atmosphere. *Journal of Geophysical Research*, 104, 12099–12111. <https://doi.org/10.1029/1998JD200091>
- Matthes, K., Funke, B., Andersson, M. E., Barnard, L., Beer, J., Charbonneau, P., & Versick, S. (2017). Solar forcing for CMIP6 (v3. 2). *Geoscientific Model Development*, 10(6), 2247–2302. <https://doi.org/10.5194/gmd-10-2247-2017>
- Mekhaldi, F., Muscheler, R., Adolphi, F., Aldahan, A., Beer, J., McConnell, J. R., et al. (2015). Multiradionuclide evidence for the solar origin of the cosmic-ray events of AD 774/5 and 993/4. *Nature Communications*, 6(1), 1–8. <https://doi.org/10.1038/ncomms9611>
- Melott, A. L., & Thomas, B. C. (2012). Causes of an AD 774–775 <sup>14</sup>C increase. *Nature*, 491(7426), E1–E2. <https://doi.org/10.1038/nature11695>
- Meul, S., Langematz, U., Kröger, P., Oberländer-Hayn, S., & Jöckel, P. (2018). Future changes in the stratosphere-to-troposphere ozone mass flux and the contribution from climate change and ozone recovery. *Atmospheric Chemistry and Physics*, 18(10), 7721–7738. <https://doi.org/10.5194/acp-18-7721-2018>
- Miyake, F., Masuda, K., Hakozaiki, M., Nakamura, T., Tokanai, F., Kato, K., et al. (2014). Verification of the cosmic-ray event in AD 993–994 by using a Japanese Hinoki tree. *Radiocarbon*, 56(3), 1189–1194. <https://doi.org/10.2458/56.17769>
- Miyake, F., Nagaya, K., Masuda, K., & Nakamura, T. (2012). A signature of cosmic-ray increase in AD 774–775 from tree rings in Japan. *Nature*, 486(7402), 240–242. <https://doi.org/10.1038/nature11123>
- Miyake, F., Suzuki, A., Masuda, K., Horiuchi, K., Motoyama, H., Matsuzaki, H., & Nakai, Y. (2015). Cosmic ray event of AD 774–775 shown in quasi-annual <sup>10</sup>Be data from the Antarctic Dome Fuji ice core. *Geophysical Research Letters*, 42(1), 84–89. <https://doi.org/10.1002/2014GL062218>
- Nissen, K. M., Matthes, K., Langematz, U., & Mayer, B. (2007). Towards a better representation of the solar cycle in general circulation models. *Atmospheric Chemistry and Physics*, 7, 5391–5400. <https://doi.org/10.5194/acp-7-5391-2007>
- NOAA (National Oceanic and Atmospheric Administration). (1976). US standard atmosphere, 1976. NOAA-S/T 76-1562, 227 pp. Retrieved from [https://www.ngdc.noaa.gov/stp/space-weather/online-publications/miscellaneous/us-standard-atmosphere-1976/us-standard-atmosphere\\_st76-1562\\_noaa.pdf](https://www.ngdc.noaa.gov/stp/space-weather/online-publications/miscellaneous/us-standard-atmosphere-1976/us-standard-atmosphere_st76-1562_noaa.pdf)
- Oberländer-Hayn, S., Meul, S., Langematz, U., Abalichin, J., & Haenel, F. (2015). A chemistry-climate model study of past changes in the Brewer-Dobson circulation. *Journal of Geophysical Research: Atmospheres*, 120, 6742–6757. <https://doi.org/10.1002/2014JD022843>
- Pavlov, A. K., Blinlov, A. V., Konstantinov, A. N., Ostryakov, V. M., Vasilyev, G. I., Vdovina, M. A., & Volkov, P. A. (2013). AD 775 pulse of cosmogenic radionuclides production as imprint of a Galactic gamma-ray burst. *Monthly Notices of the Royal Astronomical Society*, 435, 2878–2884. <https://doi.org/10.1093/mnras/stt1468>
- Pedro, J. B., Heikkilä, U. E., Klekociuk, A., Smith, A. M., vanOmmen, T. D., & Curran, M. A. J. (2011). Beryllium-10 transport to Antarctica: Results from seasonally resolved observations and modeling. *Journal of Geophysical Research*, 116(D23), D23120. <https://doi.org/10.1029/2011JD016530>
- Pedro, J. B., Smith, A. M., Simon, K. J., Van Ommen, T. D., & Curran, M. A. J. (2011). High-resolution records of the beryllium-10 solar activity proxy in ice from Law Dome, east Antarctica: Measurement, reproducibility and principal trends. *Climate of the Past*, 7(3), 707–721. <https://doi.org/10.5194/cp-7-707-2011>
- Plumb, R. A. (1996). A “tropical pipe” model of stratospheric transport. *Journal of Geophysical Research*, 101(D2), 3957–3972. <https://doi.org/10.1029/95JD03002>
- Plumb, R. A. (2002). Stratospheric transport. *Journal of the Meteorological Society of Japan*, 80, 793–809. <https://doi.org/10.2151/jmsj.80.793>
- Roeckner, E., Bäuml, G., Bonaventura, L., Brokopf, R., Esch, M., Giorgetta, M., et al. (2003). *The atmospheric general circulation model ECHAM5. Part I: Model Description*. (Vol. 349). Report / Max-Planck-Institut für Meteorologie. <http://hdl.handle.net/11858/00-001M-0000-0012-0144-5>
- Roeckner, E., Brokopf, R., Esch, M., Giorgetta, M., Hagemann, S., Kornblüehf, L., et al. (2006). Sensitivity of simulated climate to horizontal and vertical resolution in the ECHAM5 atmosphere model. *Journal of Climate*, 19, 3771–3791. <https://doi.org/10.1175/JCLI3824.1>
- Sato, T., Iwamoto, Y., Hashimoto, S., Ogawa, T., Furuta, T., Abe, S. I., et al. (2018). Features of particle and heavy ion transport code system (PHITS) version 3.02. *Journal of Nuclear Science and Technology*, 55(6), 684–690. <https://doi.org/10.1080/00223131.2017.1419890>
- Sato, T., Kataoka, R., Shiota, D., Kubo, Y., Ishii, M., Yasuda, H., et al. (2018). Real time and automatic analysis program for WASAVIES: Warning system for aviation exposure to solar energetic particles. *Space Weather*, 16(7), 924–936. <https://doi.org/10.1029/2018sw001873>
- Sigl, M., Winstrup, M., McConnell, J. R., Welten, K. C., Plunkett, G., Ludlow, F., et al. (2015). Timing and climate forcing of volcanic eruptions for the past 2,500 years. *Nature*, 523, 543–549. <https://doi.org/10.1038/nature14565>
- Škerlak, B., Sprenger, M., Pfahl, S., Tyrlis, E., & Wernli, H. (2015). Tropopause folds in ERA-Interim: Global climatology and relation to extreme weather events. *Journal of Geophysical Research: Atmospheres*, 120(10), 4860–4877. <https://doi.org/10.1002/2014JD022787>
- Sprenger, M., Maspoli, M. C., & Wernli, H. (2003). Tropopause folds and cross-tropopause exchange: A global investigation based upon ECMWF analyses for the time period March 2000 to February 2001. *Journal of Geophysical Research*, 108(D12), 8518. <https://doi.org/10.1029/2002JD002587>
- Stohl, A., Bonasoni, P., Cristofanelli, P., Collins, W., Feichter, J., Frank, A., et al. (2003). Stratosphere-troposphere exchange: A review, and what we have learned from STACCATO. *Journal of Geophysical Research*, 108(D12), 8516. <https://doi.org/10.1029/2002JD002490>

- Stohl, A., & Sodemann, H. (2010). Characteristics of atmospheric transport into the Antarctic troposphere. *Journal of Geophysical Research*, 115(D2), D02305. <https://doi.org/10.1029/2009JD012536>
- Sukhodolov, T., Usoskin, I., Rozanov, E., Asvestari, E., Ball, W. T., Curran, M. A., et al. (2017). Atmospheric impacts of the strongest known solar particle storm of 775 AD. *Scientific Reports*, 7(1), 1–9. <https://doi.org/10.1038/srep45257>
- Tost, H., Jöckel, P., Kerkweg, A., Sander, R., & Lelieveld, J. (2006). Technical note: A new comprehensive SCAVenging submodel for global atmospheric chemistry modelling. *Atmos. Chem. Phys.*, 6, 565–574. <https://doi.org/10.5194/acp-6-565-2006>
- Usoskin, I. G., & Kovaltsov, G. A. (2012). Occurrence of extreme solar particle events: Assessment from historical proxy data. *The Astrophysical Journal*, 757, 92. <https://doi.org/10.1088/0004-637X/757/1/92>
- Usoskin, I. G., Kromer, B., Ludlow, F., Beer, J., Friedrich, M., Kovaltsov, G. A., et al. (2013). The AD775 cosmic event revisited: The Sun is to blame. *Astronomy & Astrophysics*, 552, L3. <https://doi.org/10.1051/0004-6361/201321080>
- Usoskin, I. G., Solanki, S. K., Kovaltsov, G. A., Beer, J., & Kromer, B. (2006). Solar proton events in cosmogenic isotope data. *Geophysical Research Letters*, 33(8), L08107. <https://doi.org/10.1029/2006GL026059>
- Uusitalo, J., Arppe, L., Hackman, T., Helama, S., Kovaltsov, G., Mielikäinen, K., et al. (2018). Solar superstorm of AD 774 recorded subannually by Arctic tree rings. *Nature Communications*, 9(1), 1–8. <https://doi.org/10.1038/s41467-018-05883-1>
- Wesely, M. (1989). Parameterization of surface resistances to gaseous dry deposition in regional-scale numerical models. *Atmospheric Environment*, 23, 1293–1304. [https://doi.org/10.1016/0004-6981\(89\)90153-4](https://doi.org/10.1016/0004-6981(89)90153-4)
- Wong, G. J., Osterberg, E. C., Hawley, R. L., Courville, Z. R., Ferris, D. G., & Howley, J. A. (2015). Coast-to-interior gradient in recent northwest Greenland precipitation trends (1952–2012). *Environmental Research Letters*, 10(11), 114008. <https://doi.org/10.1088/1748-9326/10/11/114008>